INFLUENCE OF MODEL SPATIAL RESOLUTION ON SIMULATED AEROSOL SURFACE CONCENTRATION

by

Jessica Morena

Submitted in partial fulfillment of the
requirements for the degree of
Master of Science

at

Dalhousie University
Halifax, Nova Scotia
November 2016

This thesis is dedicated to Vlad Drobinin, for his continued and unwavering support as I pursue my goals.

Table of Contents

List of Tables

List of Figures

Abstract

Fine particulate matter known as $PM_{2.5}$ exists in Earth's atmosphere at varying levels globally. High ambient concentrations of $PM_{2.5}$ are associated with adverse health impacts, reduced visibility, and have a relatively poorly understood effect on global climate. Global chemical transport models provide an opportunity to simulate $PM_{2.5}$ with full spatial coverage on a global to regional scale. Satellite observations can be incorporated with simulated $PM_{2.5}$ to further strengthen $PM_{2.5}$ estimates. This work explores the differences in simulated $PM_{2.5}$ using fine (0.25° x 0.3125°) and coarse (2° x 2.5°) model resolution, with the aim of improving $PM_{2.5}$ estimation and monitoring.

Simulating surface concentration of $PM_{2.5}$ using fine spatial resolution improves agreement with ground-based measurements compared with a coarse resolution simulation, with explained variance increasing by as much as 0.16 seasonally. The fine resolution simulation better resolves spatial gradients in surface $PM_{2.5}$ which are poorly captured at coarse resolution, such as regions of biomass burning. In urban areas, where population is most dense and accurate health impact assessments are crucial, the fine resolution simulation reveals enhanced surface $PM_{2.5}$ at the sub-grid scale around city centres.

Combining simulated $PM_{2.5}$/AOD with satellite-derived observations yields further improvements in estimated surface $PM_{2.5}$. The fine resolution satellite-model $PM_{2.5}$ estimates show the strongest agreement with ground-based measurements, with correlation coefficients >0.53 and near 1:1 relationship across all seasons.

Differences between estimates of $PM_{2.5}$ and its constituent species at varying model resolutions result from differences in emission density, i.e. the dilution of high density emission sources over coarse grid boxes.

Recommendations for future simulations are made based on fine resolution sensitivity tests with varying chemical mechanisms and emission inputs.

List of abbreviations and symbols used

$-\nabla \bullet \mathbf{F}$	Local transport term in continuity equation (Equation 1.1).
$\partial n/\partial t$	Change in number density n with time t (Equation 1.1).
β_e	Extinction coefficient (Equations 1.2, 1.3).
η	Surface $PM_{2.5}$ to column AOD ratio.
λ	Wavelength.
ρ	Aerosol mass density (Equations 1.5, 2.2).
$\sigma^{\mathbf{ext}}_{\mathbf{dry}}$	Aerosol extinction cross section (Equation 1.6).
τ_λ	AOD at wavelength λ (Equations 1.2, 1.3).
AEIC	Aviation Emissions Inventory Code version 2.0.
AERONET	Aerosol Robotic Network.
Al	Aluminum.
AOD	Aerosol optical depth.
ARCTAS	Arctic Research of the Composition of the Troposphere from Aircraft and Satellites.
BC	Black (elemental) carbon.
BRAVO	Big Bend Regional Aerosol and Visibility Observational study.
Ca	Calcium.
CAAQS	Canadian Ambient Air Quality Standards.
CAC	Criteria Air Contaminants.
CASTNET	Clean Air Status and Tends Network.
Cl^-	Chloride.
CO	Carbon monoxide.
CTM	Chemical Transport Model.
DB	Deep Blue retrieval algorithm.
DEAD	Dust Entrainment And Deposition.
DST	Mineral dust.

DST1	GEOS-Chem dust aerosols, $r_{\text{eff}} = 0.7\,\mu\text{m}$.
DST2	GEOS-Chem dust aerosols, $r_{\text{eff}} = 1.4\,\mu\text{m}$.
DST3	GEOS-Chem dust aerosols, $r_{\text{eff}} = 2.4\,\mu\text{m}$.
DST4	GEOS-Chem dust aerosols, $r_{\text{eff}} = 4.5\,\mu\text{m}$.
DT	Dark Target retrieval algorithm.
EDGAR	Emissions Database for Global Atmospheric Research version 4.2.
EPA	Environmental Protection Agency.
$f_{\mathbf{RH}}$	Hygroscopic growth factor (Equation 2.3).
Fe	Iron.
FRM	Federal Reference Method.
GBD	Global Burden of Disease.
GC	GEOS-Chem; Goddard Earth Observing System Chemical Transport Model.
GEIA	Global Emissions Inventory Activity.
GEOS	Goddard Earth Observing System.
GEOS-FP	GEOS Forward Processing meteorological data.
GFED4	Global Fire Emissions Database version 4.1s (with small fires).
GMAO	Global Modeling and Assimilation Office.
HEMCO	Harvard-NASA Emissions Component.
$\mathbf{HNO_3}$	Nitric acid.
I_λ	Radiance; top-of-atmosphere (Equations 1.2, 1.3).
$I_\lambda(z_o)$	Radiance emitted from surface z_o to level z (Equations 1.2, 1.3).
ICOADS	International Comprehensive Ocean-Atmosphere Data Set.
IMPROVE	Integrated Monitoring of Protected Visual Environments.
L	Local sink term in continuity equation (Equation 1.1).
$L_{\mathbf{mix}}$	Aerosol mixing layer height (Equation 1.6).
M_i	Total column aerosol mass loading M (Equations 1.5, 2.2).

MAIAC	Multi-Angle Implementation of Atmospheric Correction retrieval algorithm.
MEGAN	Model of Emissions of Gases and Aerosols from Nature version 2.1.
MISR	Multiangle Imaging Spectroradiometer.
MODIS	Moderate Resolution and Imaging Spectroradiometer.
NAAQS	National AmbientAir Quality Standards.
NAPS	National Air Pollution Surveillance network.
NASA	National Aeronautics and Space Administration.
NEI2011	2011 National Emissions Inventory.
$\mathbf{NH_3}$	Ammonia.
$\mathbf{NH_4^+}$	Ammonium.
NIT	GEOS-Chem inorganic sulfur nitrates.
NO	Nitric oxide.
$\mathbf{NO_2}$	Nitrogen dioxide.
$\mathbf{NO_3^-}$	Nitrate.
$\mathbf{NO_x}$	Nitrogen oxides; includes NO, NO_2.
OC	Organic carbon.
OM	Organic mass.
P	Local source term in continuity equation (Equation 1.1).
PARANOx	Parametric Nox ship plume extension model.
$\mathbf{PM_{2.5}}$	Particulate matter with diameter $< 2.5\,\mu m$.
POA	Primary organic aerosol.
$Q_{\mathbf{ext}}$	Column-averaged extinction efficiency (Equations 1.5, 2.2).
r	Pearson correlation coefficent.
$r_{\mathbf{eff}}$	Column-averaged effective radius (Equations 1.5, 2.2).
RETRO	Reanalysis of the Tropospheric chemical composition.
SALA	GEOS-Chem accumulation mode sea salt aerosol; $r_{\text{eff}} = 0.1 - 2.5\,\mu m$.
SeaWiFS	Sea-viewing Wide Field-of-view Senser.

Si	Silicon.
SO_2	Sulfur dioxide.
SO_4^{2-}	Sulfate.
SOA	Secondary organic aerosol.
SO_x	Sulfur oxides; includes SO, SO_2.
SSa	Accumulation mode sea salt.
Ti	Titanium.
VOC	Volatile organic compound.
WHO	World Health Organization.

Acknowledgements

I would like to acknowledge Dr. Randall Martin for his support and guidance as my supervisor during my time at Dalhousie. The advice and feedback received from Randall was invaluable and I will always appreciate his interest and support in my academic pursuits. His research direction has been an inspiration and has thoroughly motivated the work contained herein.

I would also like to acknowledge all members of the Atmospheric Composition Analysis Group at Dalhousie University for assisting me throughout my research. In particular the support of Aaron van Donkelaar, Sajeev Philip, Junwei Xu, and Crystal Weagle have been of great help.

Members of the Atmospheric Chemistry Modeling Group at Harvard, notably Patrick Kim, Christoph Keller, Katie Travis, and Melissa Payer Sulprizio, have also been tremendously helpful in getting my GEOS-Chem model runs off the ground.

The GEOS-FP data used in this project have been provided by the Global Modeling and Assimilation Office (GMAO) at NASA Goddard Space Flight Center.

Computational facilities are provided by ACENET, the regional high performance computing consortium for universities in Atlantic Canada. ACENET is funded by the Canada Foundation for Innovation (CFI), the Atlantic Canada Opportunities Agency (ACOA), and the provinces of Newfoundland and Labrador, Nova Scotia, and New Brunswick.

I would also like to acknowledge my close friends and family who have supported me throughout this time. Thank you Mom, Dad, Melissa, Vlad, and Misha - this thesis would not exist without your love and support.

Chapter 1

Introduction

1.1 Background

1.1.1 Aerosols and Human Health

Small solid or liquid particles suspended in the atmosphere, known as aerosols, adversely impact human health and the natural environment in a number of ways. In addition to their indirect effect on global climate [*Boucher et al.*, 2013] and their role in reducing visibility [*Stanek et al.*, 2009], fine particulate matter with aerodynamic diameter of 2.5 µm or less ($PM_{2.5}$) is being increasingly recognized as one of the most damaging classes of air pollution to human health [*Shindell et al.*, 2012]. Due to their small diameter, $PM_{2.5}$ is able to travel deep into the lungs and enter the bloodstream, leading to a variety of afflictions including non-fatal heart attacks, irregular heartbeat, asthma, decreased lung function, increased respiratory symptoms, and premature death [*Stanek et al.*, 2009]. The Global Burden of Disease (GBD) risk assessment has ranked outdoor $PM_{2.5}$ 9th among 20 leading risk factors, with ambient particulate matter pollution accounting for 3.1 million premature deaths each year [*Lim et al.*, 2012]. In addition, as of October 2013, the International Agency for Research on Cancer has classified particulate matter as carcinogenic to humans [*Loomis et al.*, 2014], emphasizing the subtle yet powerful role $PM_{2.5}$ plays in human health and mortality.

1.1.2 $PM_{2.5}$ in North America

Increased mortality rates and instances of lung cancer, cardiopulmonary disease and diabetes are not only observed in extreme cases where annual mean $PM_{2.5}$ concentrations are very high, such as northern India ($> 60\,\mu g\,m^{-3}$) or eastern China ($> 80\,\mu g\,m^{-3}$) relative to the long-term (2001-2010) global mean of $26.4\,\mu g\,m^{-3}$ [*van Donkelaar et al.*, 2015]. Adverse effects to human health are observed globally, including in North America where long-term (2001-2010) annual mean $PM_{2.5}$ concentrations are comparatively low ($9.9\,\mu g\,m^{-3}$ for high income areas) [*van Donkelaar et al.*, 2015].

Associations between cardiovascular mortality and long-term exposure to $PM_{2.5}$ have been reported for concentrations as low as a few micrograms per cubic meter, with no evidence of a lower exposure limit below which health impacts are not detected [*Crouse et al.*, 2012]. Adverse health impacts caused by fine aerosols can be diminished by reducing exposure to $PM_{2.5}$, with as little as a $10\,\mu g\,m^{-3}$ decrease resulting in a 0.35 to 0.61 year increase in life expectancy [*Correia et al.*, 2013; *Pope III et al.*, 2009]. Accurate monitoring, assessment, and regulation of $PM_{2.5}$ is critical in achieving such a reduction and can lead to measurable improvements in human health and mortality on a global scale.

1.2 Measuring $PM_{2.5}$

Global air quality guidelines for particulate matter have been established by the World Health Organization (WHO) based on the lower end of the range at which $PM_{2.5}$ exposure is associated with adverse health impacts. Based on this criteria, the WHO adopted a long-term guideline for annual average $PM_{2.5}$ concentration of $10\,\mu g\,m^{-3}$ and a short-term (24-hour) guideline of $25\,\mu g\,m^{-3}$ [*World Health Organization*, 2006]. Air quality standards also exist at the national level for many countries including Canada and the United States.

The United States National Ambient Air Quality Standard (NAAQS) set by the US Environmental Protection Agency (EPA) is slightly less strict than the WHO guideline, with a short-term (24-hour) standard of $35\,\mu g\,m^{-3}$ and a long-term guideline of $12\,\mu g\,m^{-3}$ [*US EPA Office of Air Quality Planning and Standards*, 2016c]. The Canadian Ambient Air Quality Standard (CAAQS) for $PM_{2.5}$ provides a more ambitious national standard of $28\,\mu g\,m^{-3}$ for short-term and $10\,\mu g\,m^{-3}$ for long term [*Canadian Council of Ministers of the Environment*, 2014]. In recent years, from 2010 to 2012, the majority of locations reporting $PM_{2.5}$ concentrations in Canada recorded concentrations below the 24-hour target, with only three locations in British Columbia and five locations in Alberta exceeding the limit, likely due to seasonal forest fires [*Canadian Council of Ministers of the Environment*, 2014]. The success thus far in reducing $PM_{2.5}$ concentration demonstrates the powerful response to the implementation of global and nation-wide air quality standards for $PM_{2.5}$. It is therefore crucial that standards continue to provide ambitious goals for nations to adhere to in order

to minimize the adverse health impacts observed even at low $PM_{2.5}$ exposure levels.

Adherence to air quality standards is contingent upon accurate measurement and monitoring of ambient $PM_{2.5}$ levels. Figure 1.1 illustrates three $PM_{2.5}$ assessment methods along with their relative strengths and weaknesses, as described below.

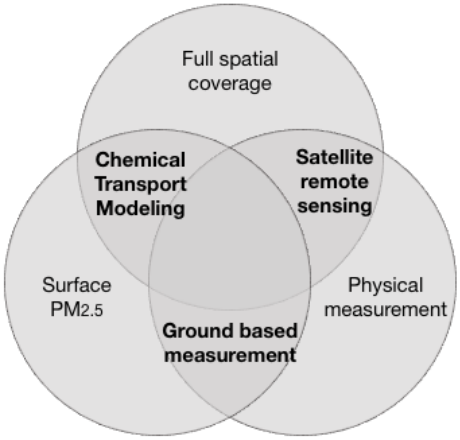

Figure 1.1 Relative strengths and weaknesses of three $PM_{2.5}$ assessment methods

1.2.1 Ground-based Measurement of $PM_{2.5}$

Adherence to global and national-level air quality standards is monitored via ground-based measurement of $PM_{2.5}$ and its constituents - sulfate, nitrate, ammonium, organic aerosols, black carbon, mineral dust, and sea salt. In situ monitoring is highly valuable and often considered "truth" in $PM_{2.5}$ exposure and estimation studies (e.g. *van Donkelaar et al.*, 2015, *Philip et al.*, 2014a). While networks of monitoring stations are present in various locations worldwide, their locations are not evenly spatially distributed and are frequently sparsely located. In addition to having poor spatial coverage, monitoring stations are only capable of taking point measurements, which may or may not be representative of the surrounding area. While studies have found geostatistical interpolation between monitors to provide accurate estimates of $PM_{2.5}$ in regions where monitoring networks are dense, they struggle to represent $PM_{2.5}$ between sites in many parts of the world where monitoring locations are sparse [*Pinto et al.*, 2004; *Lee et al.*, 2012]. A full understanding of the adverse impacts of aerosols including $PM_{2.5}$ requires an understanding of aerosol emissions, deposition, transport, and chemistry at high spatial and temporal resolution [*Arunachalam*

et al., 2011]. Such high resolution data cannot be provided from ground-based measurements alone.

1.2.2 Chemical Transport Models to Estimate $PM_{2.5}$

Chemical transport models (CTMs) are an important quantitative tool for simulating atmospheric chemistry, allowing for an enhanced understanding of the relationship between primary particulates and secondary particulate precursors to ambient $PM_{2.5}$ concentrations. Eulerian box models describe a subset of CTMs in which chemical production and loss occur over time within a stationary grid box (Figure 1.2; *Jacob* [1999]). CTMs compute aerosol concentration in each box by solving the continuity equation (Equation 1.1). The continuity equation computes the change in number density of each tracer n over time t ($\partial n/\partial t$) by subtracting losses due to chemistry and deposition (L) and a transport term representing losses from the box via transport ($-\nabla \bullet \mathrm{F}$), from sources such as emission, chemical production, and transport into the box (P).

$$\frac{\partial n}{\partial t} = P - \nabla \bullet \mathrm{F} - L \tag{1.1}$$

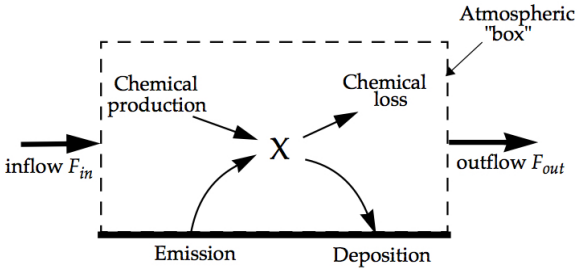

Figure 1.2 Theoretical basis for Eulerian box models [*Jacob*, 1999]

$PM_{2.5}$ and model resolution

The horizontal spatial resolution of CTMs, as determined by the resolution of their meteorological input fields, can have a strong influence on simulation output. Studies have found that coarse resolution models underpredict the adverse health impacts attributed to $PM_{2.5}$ relative to fine scale simulations. Comparisons of simulations

at fine and coarse resolution have shown coarse simulations to underpredict $PM_{2.5}$-attributed mortality estimates by 8 to 11%, or approximately 12,000 deaths per year when considering a 3- to 4-fold increase in spatial resolution [*Punger and West*, 2013; *Li et al.*, 2015]. When resolution is changed drastically, for example from a typical global scale of 250 km (2.5°) to a community scale of 12 km (0.1°), mortality rates can be underpredicted by as much as 40% [*Punger and West*, 2013].

Underprediction of $PM_{2.5}$-related health effects follows from a low bias in model-predicted $PM_{2.5}$ surface concentration. Simulations using larger grid cells can lead to dilution of point source emissions and underestimation of other sub-grid scale processes. Population-dense areas where emissions are likely to be enhanced relative to surrounding rural areas may therefore be misrepresented due to spatial averaging of emissions causing underestimation of $PM_{2.5}$ concentration in urban centres and overestimation in rural areas [*Thompson et al.*, 2014]. Thus, coarse models underestimate $PM_{2.5}$ most significantly in highly populated urban centres [*Li et al.*, 2015].

The influence of model spatial resolution on predicted $PM_{2.5}$ surface concentration is influenced by a number of factors. While resolution of model output is driven by the resolution of the meteorological input data, *Cuvelier et al.* [2013] found that approximately 70% of the simulated particulate matter response to grid resolution results from differences in emission density. It is therefore critically important to provide the model with accurate, fine resolution emissions data in order to precisely resolve $PM_{2.5}$ concentration around urban centres. Seasonality also plays a role in the influence of model resolution on $PM_{2.5}$ prediction, with resolution playing a modest role in summer but becoming more significant in the winter months at northern mid-latitudes [*Fountoukis et al.*, 2013]. Different species are also affected differently by resolution. The species most likely to be underpredicted at coarse model resolution are those with short lifetimes, and therefore small dispersal ranges [*Punger and West*, 2013]. Primary species such as elemental and organic carbon also show greater bias with changing spatial resolution than secondary species such as sulfate, nitrate, and ammonium [*Punger and West*, 2013; *Thompson et al.*, 2014; *Fountoukis et al.*, 2013; *Li et al.*, 2015].

1.3 Satellite Observations to Estimate $PM_{2.5}$

While CTMs can provide full global coverage in estimated $PM_{2.5}$ concentration, imposing a physical constraint can improve the accuracy of such estimates. Ground-based monitors provide one measure against which models can be validated, however their sparse geographic coverage limits their predictive ability. Satellite instrumentation is another source for physical measurements which can constrain model $PM_{2.5}$ estimates. Full global coverage is an advantage of satellite data, however rather than measuring surface $PM_{2.5}$ concentration directly, remote sensing records observations of the entire atmospheric column through measurement of aerosol optical depth.

Aerosol optical depth (AOD) is a measure of the extinction of light in the atmospheric column as it is absorbed and scattered by ambient aerosols. Satellite remote sensing observes total column AOD by measuring radiance as seen from the top of the atmosphere and using retrieval algorithms to relate these observations to AOD. Equations 1.2 and 1.3 provide a simplified explanation of the relationship between measured radiance at a given wavelength (I_λ),and column AOD (τ_λ).

$$I_\lambda = I_\lambda(z_o) \exp\left[-\int_{z_o}^{\infty} \beta_e(z')dz'\right] \tag{1.2}$$

$$\tau_\lambda \equiv \int_{z_o}^{\infty} \beta_e(z')dz' = -\ln\left[\frac{I_\lambda}{I_\lambda(z_o)}\right] \tag{1.3}$$

where I_λ is the radiance measured at the top of the atmosphere, $I_\lambda(z_o)$ is the radiance emitted from level z_o (the surface for total column AOD), β_e is the extinction coefficient with units of inverse length (i.e. m^{-1}), a factor relying on the properties of the medium and the wavelength of the incident radiation (λ). It can be seen from Equation 1.3 that AOD is related to the ratio of the logarithm of radiance at the top of the atmosphere to that at the bottom of the atmosphere. In theory, the radiation observed at the top of Earth's atmosphere will have a different spectral signature than surface radiance. Multiple wavelength bands (i.e. visible, near infrared, and shortwave wavelength regions) can be used to infer physical properties of the observed aerosols based on measurement of outgoing radiation [*Levy et al.*, 2013].

This seemingly simple relationship is complicated by the fact that there is not a single source of radiation from the lower surface (z) being transmitted to the top of the atmosphere to be observed by the satellite, but rather a combination of absorption and

scattering by the surface, atmosphere, and clouds (Figure 1.3; *Hoff and Christopher* [2009]). Satellite retrievals of AOD can therefore become quite complex and require physical and observational assumptions about the surface and expected aerosol types above the surface [*Levy et al.*, 2013].

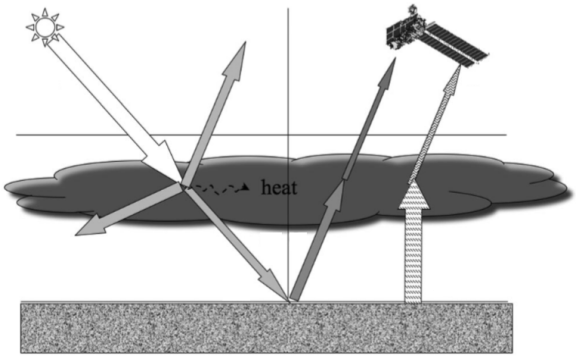

Figure 1.3 Various sources of radiance (represented by arrows) absorbed, scattered, and emitted by Earth's surface and atmosphere are observed by satellite instrumentation as top-of-atmosphere radiance [*Hoff and Christopher*, 2009]

.

Obtaining $PM_{2.5}$ estimates from satellite AOD observations requires a characterization of the complex relationship between surface and total column aerosol concentrations. The surface-to-column relationship can be characterized by a conversion factor η, as expressed in Equation 1.4 [*van Donkelaar et al.*, 2010].

$$PM_{2.5} = \eta \times \text{AOD} \tag{1.4}$$

The relationship between column AOD for tracer i at a given level in the atmosphere and the mass of tracer in that level M_i [$\mu g\, m^{-2}$] can be expressed in terms of the Mie extinction efficiency ($Q_{\text{ext,dry,i}}$), a factor accounting for hygroscopic particle growth (f_{RH}), dry aerosol effective radius ($r_{\text{eff,dry,i}}$, [m^2]), and species density (ρ_i, [$\mu g\, m^{-3}$]) as in Equation 1.5. Total column AOD is the sum of $\text{AOD}_{\text{i,lev}}$ for all species i over all vertical levels in the atmosphere.

$$\text{AOD}_{i,\text{lev}} = \frac{3}{4}\frac{Q_{\text{ext}i}\ f_{\text{RH}}}{r_{\text{eff}i}\ \rho_i} M_i \tag{1.5}$$

The above equation can be rewritten as in *Chu et al.* [2013] to express η in terms of the hygroscopic growth factor (f_{RH}), aerosol extinction cross-section per unit mass ($\sigma^{\text{ext}}_{\text{dry}}$, [$m^2\, \mu g^{-1}$]) and aerosol mixing layer height (L_{mix}, [m]), where M_i in Equation

1.5 is equivalent to the $PM_{2.5}$ concentration times the mixing layer height. The aerosol mixing layer height is defined as the upper boundary of the lowest layer of the troposphere where atmospheric mixing is influenced by the Earth's surface.

$$\eta = \frac{PM_{2.5}}{AOD} = \frac{1}{L_{mix}\ [f_{RH}\ \sigma^{ext}_{dry}]_{surface}} \tag{1.6}$$

Equation 1.6 illustrates that η varies with relative humidity, aerosol type, aerosol size, and mixing layer height. The surface-to-column ratio η can be estimated by a CTM and then applied to satellite observations of AOD to infer surface-level $PM_{2.5}$ concentration. Such estimates can be validated with ground-based measurements.

This study aims to explore the effect of model resolution on $PM_{2.5}$ estimates and how this influences satellite-derived estimates of $PM_{2.5}$ (i.e. effect of resolution on $PM_{2.5}$/AOD), particularly in urban regions where prediction accuracy for health impact assessments is crucial.

Chapter 2

Methods

2.1 Global Chemical Transport Modeling: GEOS-Chem

GEOS-Chem (GC) version 10-01 [*Bey et al.*, 2001], a global 3-dimensional chemical transport model, was used to simulate concentrations of $PM_{2.5}$ constituents including sulfate, nitrate, ammonium, carbonaceous aerosols, mineral dust, sea salt, and secondary organic aerosols. Aerosol optical depth (AOD) of sulfate, carbonaceous aerosols, dust, and sea salt at 550 nm wavelength was also computed.

2.1.1 Meteorological Data and Spatial Resolution

GC is driven by assimilated meteorological data from the Goddard Earth Observation System (GEOS) of the NASA Global Modeling and Assimilation Office (GMAO). Several meteorological data products exist for use within the GEOS-Chem framework, including GEOS-FP which was the product used for this study. GEOS-FP is GMAOs most recent product (as of this writing), with data available from April 2012 to present day. GEOS-FP meteorological data includes parameters such as wind speed, temperature, humidity, cloud fraction, and precipitation at an hourly temporal resolution. Three-dimensional quantities such as upper air properties are also included at a 3-hourly temporal resolution.

Presently, the finest horizontal spatial resolution at which global simulations can be performed by GEOS-Chem is 2° x 2.5°, approximately 150 km x 200 km at 45° latitude (see Figure 2.1 (left)). At this resolution, the model is able to resolve broad regions but unable to discern smaller areas, including large urban centres. GEOS-Chem offers finer resolution nested-grid simulations over four large global regions including North America, Europe, China, and Southeast Asia. GC nested-grid simulations can be performed at a horizontal spatial resolution as fine as 0.25° x 0.3125°, approximately 20 km x 25 km at 45° latitude (see Figure 2.1 (right)). At such fine resolution, the spatial distribution of surface-level $PM_{2.5}$ and its constituents can be resolved over urban centres, providing more detailed information regarding surface

air quality in such regions.

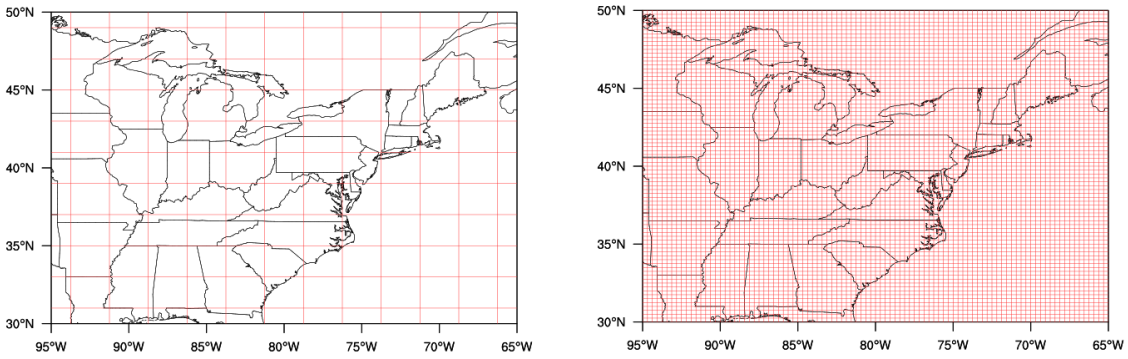

Figure 2.1 GEOS-Chem horizontal spatial resolution 2° x 2.5°(left); 0.25° x 0.3125°(right)

A vertical grid consisting of 47 pressure levels extending from the surface (1013.25 hPa) to the top of atmosphere (0.01 hPa) was used for fine and coarse resolution simulations. Vertical grid boxes are distributed by atmospheric pressure. The bottommost layer, taken here to represent the surface, corresponds to approximately the lowest 7.6 hPa, or 60 m, of the atmosphere.

2.1.2 Emission Inventories

GEOS-Chem v10-01 implements the Harvard-NASA Emissions Component (HEMCO), a stand-alone software component which computes emissions in global CTMs [*Keller et al.*, 2014]. HEMCO provides an interface which allows the user to easily configure which emissions inventories to use for a given simulation. Emission inventories used in this study are outlined in Table 2.1.

Anthropogenic emissions of NO_x, CO, SO_2, and NH_3 are provided by regional inventories where data are available, including the Big Bend Regional Aerosol and Visibility Observational study (BRAVO) for Mexico [*Kuhns et al.*, 2001], the Criteria Air Contaminants (CAC) for Canada [*Environment and Climate Change Canada*, 2016a], and the 2011 National Emissions Inventory (NEI2011) for the United States [*US EPA Office of Air Quality Planning and Standards*, 2016d]. The NEI2011 inventory extends into Canada and Mexico (see Figure A.1) and is given priority over CAC and BRAVO in areas where regional inventories overlap. Emissions Database for Global Atmospheric Research (EDGAR) version 4.2 global anthropogenic emissions were used when regional inventories were not available. In this study, NEI2011

was used up to the end of 2013 after which GEOS-Chem defaults to EDGAR.

Volatile organic compound (VOC) emissions come from the Reanalysis of the Tropospheric chemical composition (RETRO) inventory [*Schultz et al.*, 2008; *Reinhart and Millet*, 2011]. Biogenic VOCs come from the Model of Emissions of Gases and Aerosols from Nature version 2.1 (MEGAN), including monoterpenes and secondary organic aerosols [*Guenther et al.*, 2012]. Biomass burning emissions are provided at a 3-hourly temporal resolution by the Global Fire Emissions Database version 4.1s (GFED4) with small fires [*Giglio and Randerson*, 2013; *van der Werf et al.*, 2010]. The Mineral Dust Entrainment and Deposition (DEAD) extension was used for mineral dust emissions [*Fairlie et al.*, 2010, 2007; *Zender*, 2003]. Ship emission of SO_2 come from the Arctic Research of the Composition of the Troposphere from Aircraft and Satellites (ARCTAS) inventory [*Eyring et al.*, 2005], CO from the International Comprehensive Ocean-Atmosphere Data Set (ICOADS) [*Wang et al.*, 2008], and NO_x from PARANOx [*Vinken et al.*, 2011]. Aircraft emissions come from the Aviation Emissions Inventory Code version 2.0 (AEIC) [*Stettler et al.*, 2011].

Base emissions are constructed from external data using bottom-up (e.g. known rates of fuel consumption) or top-down (e.g. atmospheric observations) approaches. Scale factors are applied to account for diurnal, day of the week, seasonal or annual variability relative to the base emissions [*Keller et al.*, 2014]. For example, the regional anthropogenic inventory for North America (NEI2011) uses base emissions from 2011 and scales emitted species with an annual scale factor based on United States emissions the National Emissions Inventory Air Pollutant Emissions Trends Data [*US EPA*, 2016].

Spatial resolution of emission inventories plays a large role in model response to grid resolution. An intercomparison study of five CTMs found that approximately 70% of the model response in predicted particulate concentrations to changing grid resolution was determined by differences in emission strengths [*Cuvelier et al.*, 2013]. Spatial resolution of emission inventories used in this study are listed in Table 2.1.

2.1.3 GEOS-Chem Model Runs Conducted

GEOS-Chem version 10-01 was used to simulate surface aerosol concentrations including sulfate, nitrate, ammonium, carbonaceous aerosol, mineral dust, and sea salt.

Table 2.1 Emission inventories used in GEOS-Chem

Inventory	Species	Resolution (lat x lon)	Reference
Anthropogenic emissions			
EDGAR v4.2	NO CO SO_x NH_3	0.1° x 0.1°	*Muntean et al.*, 2014
NEI2011	NO_x CO SO_x NH_3 OC BC SOA	0.1° x 0.1°	*US EPA Office of Air Quality Planning and Standards*, 2016d
CAC	NO CO SO_x NH_3	1° x 1°	*Environment and Climate Change Canada*, 2016a
BRAVO	NO CO SO_x	1° x 1°	*Kuhns et al.*, 2001
GEIA	NH_3	1° x 1°	*Benkovitz et al.*, 1996
Aircraft emissions			
AEIC	NO_2 CO	1° x 1°	*Stettler et al.*, 2011
Ship emissions			
ARCTAS	SO_2	1° x 1°	*Eyring et al.*, 2005
ICOADS	CO NO	1° x 1°	*Wang et al.*, 2008
Biofuel/biomass burning emissions			
GFED4.1s, 3 hourly	NO CO OC BC SOA	0.25° x 0.25°	*Giglio et al.*, 2013; *van der Werf et al.*, 2010
BIOFUEL	NO CO SO_2 SOA	4° x 5 °	*Yevich and Logan*, 2014
Biogenic emissions			
MEGAN	SOA	1° x 1°	*Guenther et al.*, 2012
Misc. natural emissions			
Volcano	SO_2	1° x 1°	*Diehl et al.*, 2012
Lightning NOx	NO_x	0.25° x 0.3125°	*Murray et al.*, 2012
Soil NOx	NO_x	0.25° x 0.25°	*Hudman et al.*, 2012
DEAD	Dust	4° x 5°	*Fairlie et al.*, 2010, 2007; *Zender*, 2003

Column aerosol optical depth (AOD) for the same species at a wavelength of 550 nm was also determined. Simulations were conducted for a run period of 2 years, from May 2013 to May 2015. The dates were chosen based on data availability in the GEOS-FP meteorological datasets (data available from April 2012 - present). A global simulation was conducted at 2° x 2.5° and a regional nested grid simulation over North America was conducted at 0.25° x 0.3125°, covering from 10° to 70° latitude and -140° to -70° longitude as defined by nested grid boundaries. For the 0.25° x 0.3125° simulation transport and convection were computed every 5 minutes, emissions and chemistry were computed every 15 minutes. For the 2° x 2.5° simulation transport and convection were computed every 15 minutes, emissions and chemistry were computed every 30 minutes. Both runs used GEOS-FP meteorological input data.

2.1.4 Modifications to Standard GEOS-Chem code

Previous studies have reported an over-prediction of nitrate by GEOS-Chem when compared with measurements from the IMPROVE network [*Heald et al.*, 2012; *Zhang et al.*, 2012]. A 75% artificial reduction in simulated HNO_3 concentration at each

chemistry timestep was found to bring surface nitrate (NO_3^-) concentration near agreement with ground-based measurements at a spatial resolution of 0.5° x 0.667° with a 20-minute chemistry timestep [*Heald et al.*, 2012]. This reduction was scaled to the model resolutions used in this research, resulting in the same reduction in HNO_3 over an equivalent amount of time. In the 2° x 2.5° simulation, HNO_3 concentrations were reduced to 62.5% of their simulated values at each 30-minute chemistry timestep. For the 0.25° x 0.3125° simulation, HNO_3 was reduced to 87.5% at each 10-minute chemistry timestep. These reductions are equivalent to a 75% reduction every 20 minutes of simulated model time, as in *Heald et al.* [2012]. Refer to Appendix Figure A.3 for effect of HNO_3 reduction on simulated NO_3^-.

2.1.5 Model Output Variables of Interest

The model was run at coarse (2° x 2.5°) and fine (0.25° x 0.3125°) resolution and a number of output variables were examined. The primary variables of interest were the mixing ratios of the species which comprise $PM_{2.5}$, including sulfate (SO4), inorganic nitrate (NIT), ammonium (NH4), hydrophilic and hydrophobic organic carbon (OCPI, OCPO), hydrophilic and hydrophobic black carbon (BCPI, BCPO), secondary organic aerosols (SOA), mineral dust (DST), and accumulation mode sea salt (SALA).

Simulated organic carbon concentrations were converted to organic mass using a spatially and seasonally resolved ratio (OM/OC) which describes the relationship between organic mass and organic carbon [*Philip et al.*, 2014b]. Organic mass is the component of $PM_{2.5}$ consisting primarily of organic carbon in addition to other elements such as oxygen, hydrogen, and nitrogen. The relationship between OM and OC varies with sources of primary (POA) and secondary (SOA) organic aerosols as well as their degree of ageing. POA is produced mainly by combustion sources; SOA is formed through oxidation and partitioning of volatile organic compounds (VOCs) emitted by both anthropogenic and biogenic sources [*Philip et al.*, 2014b]. The ratio OM/OC ranges from 1.69 to 2.29 with a mean value of approximately 2.24 over North America. OM/OC is lower for regions where POA dominates over SOA and when POA is oxidized slowly, i.e. northeastern US in winter. Figure 2.2 shows the seasonal and spatial distribution of OM/OC. SOA and POA were combined to obtain total

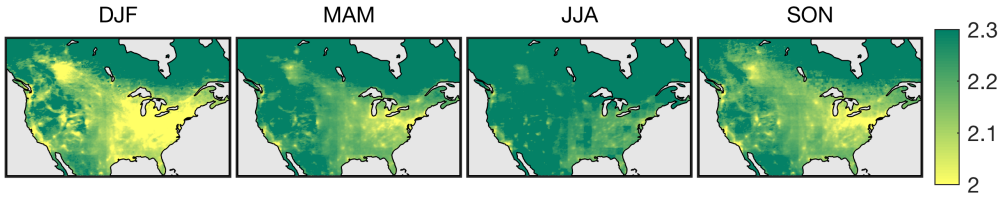

Figure 2.2 Ratio of OM/OC over North America. Ratio increases with organic aerosol ageing and is lower for regions where POA dominates over SOA.

simulated organic mass.

Mineral dust is simulated by GEOS-Chem into four size bins based on effective radius (DST1, DST2, DST3, DST4). The smallest size bin (DST1) represents dust aerosols with an effective radius below 0.7 µm, the second smallest bin (DST2) represents dust aerosol with an effective radius between 0.7 and 1.4 µm. Since DST2 contains aerosols both smaller and larger than the 2.5 µm diameter threshold for $PM_{2.5}$, only a fraction of this value is included in the sum for $PM_{2.5}$. Based on the dust size distribution, the recommended fraction of DST2 to include in $PM_{2.5}$ calculations is 38%.

When comparing individual species to ground-based measurements, individual species were treated at relative humidity (RH) of 0%. EPA measurement standards for total $PM_{2.5}$ are conducted at a RH of 35% [*Chow and Watson*, 1998], therefore a species-independent growth factor must be applied to hydrophilic species to account for growth due to uptake of water. These growth factors represent aerosol hygroscopicity as used in GEOS-Chem [*Harvard Atmospheric Chemistry and Modeling Group*, 2016] and are stated in bold in Equation 2.1.

Surface $PM_{2.5}$ from GEOS-Chem

Surface $PM_{2.5}$ was calculated as the sum of the concentrations of the species listed above, along with the considerations described in the previous section (conversion of OC to OM, 38% of DST2 dust bin, and hygroscopic growth factors for RH of 35%) as found in the lowest vertical model level (i.e. surface). Note that hygroscopic growth of hydrophilic black carbon is built into the model with a growth factor of 1.8 for relative humidity of 35% [*GEOS-Chem Support Team*, 2014].

$$
\begin{aligned}
\mathrm{PM}_{2.5} = & \mathbf{1.33}\ (\mathrm{SO4} + \mathrm{NIT} + \mathrm{NH4}) \\
& + \tfrac{\mathrm{OM}}{\mathrm{OC}}\ (\mathbf{1.12}\ \mathrm{OCPI} + \mathrm{OCPO}) + \mathbf{1.12}\ \mathrm{SOA} \\
& + (\mathrm{BCPI} + \mathrm{BCPO}) \\
& + (\mathrm{DST1} + 0.38\ \mathrm{DST2}) \\
& + \mathbf{1.86}\ \mathrm{SSa}
\end{aligned}
\tag{2.1}
$$

Column AOD from GEOS-Chem

Column AOD for each tracer i at each vertical level was calculated as in Equation 2.2 (recall from Section 1.3).

$$\mathrm{AOD}_{i,\mathrm{lev}} = \frac{3}{4}\frac{Q_{\mathrm{ext},i}\ f_{\mathrm{RH}}}{r_{\mathrm{eff},i}\ \rho_i} M_i \tag{2.2}$$

The hygroscopic growth factor (f_{RH}) is the ratio of wet to dry effective radius for a given particle at a given relative humidity (Equation 2.3). Aerosol optical properties at high spectral resolution for calculations with GEOS-Chem data including Q_{ext} and r_{eff} are available on the GEOS-Chem website [*GEOS-Chem Support Team*, 2014].

$$f_{\mathrm{RH}} = \frac{r_{\mathrm{eff},\mathbf{wet}}, i}{r_{\mathrm{eff},\mathbf{dry}}, i} \tag{2.3}$$

Total column AOD was then taken to be the sum of AOD for all species i from the lowest model level (surface) up to level 35 ($\sim$100 hPa).

$$\mathrm{AOD}_{\mathrm{column}} = \sum_{\mathrm{lev}=1}^{35} \sum_{i=1}^{\mathrm{tracers}} \mathrm{AOD}_{i,\mathrm{lev}} \tag{2.4}$$

2.2 Satellite Measurements

The observed AOD used in this study is a combined product which incorporates satellite AOD from eight sources along with model values and ground-based measurements from the Aerosol Robotic Network (AERONET) to adjust the relative contribution of each source. Sources of satellite data are listed in Table 2.2 and described in further detail in the remainder of Section 2.2. Locations with reduced satellite sampling, such as northern regions with seasonal snow cover or tropical southeast Asia where cirrus

clouds can interfere with sampling, are incorporated into the combined product by using simulated values [*van Donkelaar et al.*, 2016].

Table 2.2 Observational sources for combined AOD product

Satellite	Instrument	Retrieval Algorithm
Terra	MISR	MISR
Terra	MODIS	Dark Target
Terra	MODIS	Deep Blue
Terra	MODIS	MAIAC
Aqua	MODIS	Dark Target
Aqua	MODIS	Deep Blue
Aqua	MODIS	MAIAC
SeaStar	SeaWiFS	Deep Blue

2.2.1 Satellites

The Terra and Aqua satellites are both operated by NASA. Terra has been in orbit since 2000 and Aqua since 2002 [*Remer et al.*, 2008] and are both presently still in orbit. Terra has a descending orbit (north to south) and passes the equator in the morning at approximately 10:30 A.M. local time, while Aqua has an ascending orbit (south to north) and passes the equator in the afternoon at approximately 1:30 P.M. local time. These instruments work together to optimize cloud-free surface viewing with near-daily global coverage [*Savtchenko et al.*, 2004].

The SeaStar spacecraft launched in 1997 and stopped collecting data in late 2010. SeaStar follows a descending orbit (north to south) and passes the equator at approximately 12:00 P.M. local time. SeaStar takes approximately one week for complete global coverage [*NASA Goddard Space Flight Center; SeaWiFS*, 2016].

2.2.2 Satellite Instruments

The theoretical basis for passive retrievals of AOD is outlined in Section 1.3. AOD from four passive satellite instruments are used in the combined product - MODerate resolution Imaging Spectroradiometer (MODIS) on board the Terra and Aqua satellites, the Multiangle Imaging SpectroRadiometer (MISR) on board Terra, and the

Sea-viewing Wide Field-of-view Sensor (SeaWiFS) inboard the SeaStar spacecraft.

MODIS has a swath width of 2330 km, a spectral range from 412 nm to 1450 nm in 36 bands, and a fine spatial resolution of 250 m at nadir [*NASA Goddard Space Flight Center; MODIS*, 2016].

MISR has a swath width of 380 km, a spectral range from 446 nm to 866 nm in four bands, and a nadir spatial resolution of 1.1 km. MISR utilizes nine sensors to collect imaging data from multiple widely-spaced angles, providing data which can more easily distinguish between different types of aerosols, cloud forms, and land surface covers [*NASA Jet Propulsion Laboratory; MISR*, 2016].

SeaWiFS has a swath width of 1500 km, a spectral range from 402 nm to 885 nm in 8 bands, and a nadir spatial resolution of 1.1 km. Initially created for ocean-color observing, additional products including AOD have been produced from observed radiance [*NASA Goddard Space Flight Center; SeaWiFS*, 2016].

2.2.3 Retrieval Algorithms

The MODIS Collection 6 Dark Target (DT) retrieval algorithm was developed to infer aerosol properties over surfaces with low surface reflectance in the visible and shortwave infrared parts of the spectrum. This algorithm works best over visually "dark" surfaces where aerosols appear to brighten the scene, as observed from above [*Levy et al.*, 2010].

The MODIS Deep Blue (DB) algorithm retrieves aerosol properties over bright surfaces such as broad desert regions and urban areas. The basic principle is that these areas are bright in the near infrared and visible parts of the spectrum, while much darker in the blue spectral region [*Hsu et al.*, 2004].

The Multi-Angle Implementation of Atmospheric Correction (MAIAC) retrieval algorithm simultaneously retrieves aerosol information over land and a surface bidirectional reflectance factor. A time series of image-based MODIS data combines multiple single-view passes to provide multi-angle coverage for surface grid cells. MAIAC has been shown to improve accuracy in retrievals over bright surfaces over DT/DB algorithms [*Lyapustin et al.*, 2011].

The MISR retrieval algorithm relies on lookup tables of atmospheric radiative

parameters and predetermined aerosol mixture models. It utilizes multi-angle observations to compare top-of-atmosphere radiance with surface radiance, utilizing model radiances calculated for a variety of aerosol compositions and size distributions [*Martonchik et al.*, 1998]. MAIAC performs well for difficult surface conditions such as mountainous regions [*van Donkelaar et al.*, 2016].

Combining a number of satellite retrievals and algorithms, along with an adjustment based on ground-level AERONET observations, provides thorough spatial and temporal coverage for a more complete AOD product than a single satellite retrieval alone could provide.

2.3 Ground-based Monitoring of $PM_{2.5}$

2.3.1 Measurement Networks

Ground-based monitoring of $PM_{2.5}$ and its constituent species were used in this study as a measure of "true" aerosol concentration against which model performance was measured. Networks of monitoring stations used include the Canadian National Air Pollution Surveillance Network (NAPS) for Canada [*Environment and Climate Change Canada*, 2016b], the Integrated Monitoring of Protected Visual Environments (IMPROVE) [*US Federal Land Manager Environmental Database*, 2016], Clean Air Status Trends Network (CASTNET) [*US EPA Office of Air Quality Planning and Standards*, 2016a], and EPA Federal Reference Method (FRM) monitoring sites for the United States [*US EPA Office of Air Quality Planning and Standards*, 2016b].

2.3.2 Speciation Data

Concentrations of the constituent species which make up $PM_{2.5}$ are also of interest, thus ground-based measurements are required to evaluate model performance at simulating these species. These species, or tracers, include sulfate (SO_4^{2-}), nitrate (NO_3^-), ammonium (NH_4^+), organic mass (OM), black/elemental/light absorbing carbon (BC), mineral dust (DST), and accumulation mode sea salt (SSa).

Most species were measured directly by the speciation monitoring networks, with the exception of organic mass, mineral dust and salt which were calculated for this study from other measured species using equations stated in Table 2.3.

Table 2.3 $PM_{2.5}$ constituent tracer calculations from in situ measured data

Species	Equation	Reference
OM	$(\frac{OM}{OC} \times OC)$	*Philip et al.*, 2014b
Dust	$(2.20 \times Al) + (2.49 \times Si) + (1.63 \times Ca) + (2.42 \times Fe) + (1.84 \times Ti)$	*Malm et al.*, 1994
Salt	$1.8 \times Cl^-$	*Pitchford et al.*, 2007

Chapter 3

Results and Discussion

3.1 Surface $PM_{2.5}$

Surface $PM_{2.5}$ measured by ground-based monitoring networks is shown in the right column of Figure 3.1. High surface concentrations typically occur in areas with high emissions, such as urban or industrialized regions, or where meteorological conditions such as atmospheric stability inhibits atmospheric mixing. These effects are observed in Figure 3.1 over the eastern United States where measured $PM_{2.5}$ concentration is relatively high over regions of high population density and industrial activity, and thus greater anthropogenic emissions.

Seasonal variability in $PM_{2.5}$ is also observed with highest surface concentrations occurring in the summer months. Secondary aerosol concentration from species such as sulfate and nitrate is enhanced in the summer months when photochemistry is strongest, leading to relatively high summertime $PM_{2.5}$ [*Malm et al.*, 1994]. Biogenic aerosol emission is also greater in the summer months, leading to higher $PM_{2.5}$ concentrations [*Goldstein et al.*, 2009].

GEOS-Chem simulations of surface $PM_{2.5}$ at both fine and coarse model resolution capture seasonal variability, however concentrations over the eastern United States during winter months are relatively high compared to summer months when one would expect higher concentrations. A potential missing source of SOA due to oxidation of VOCs above the surface layer in the summer months in the model may account for weak seasonality in simulated $PM_{2.5}$ [*Ford and Heald*, 2013].

Agreement between simulated and measured concentration is strongest in the spring (r = 0.49, 0.63 for coarse, fine resolution respectively) and summer months (r = 0.48, 0.58 for coarse, fine resolution respectively). Using fine resolution results in an improvement in correlation strength for all seasons as compared to coarse resolution, with the smallest improvement in r occurring in fall (0.06 increase in explained variance) and the greatest improvement occurring in spring (0.16 increase in explained variance).

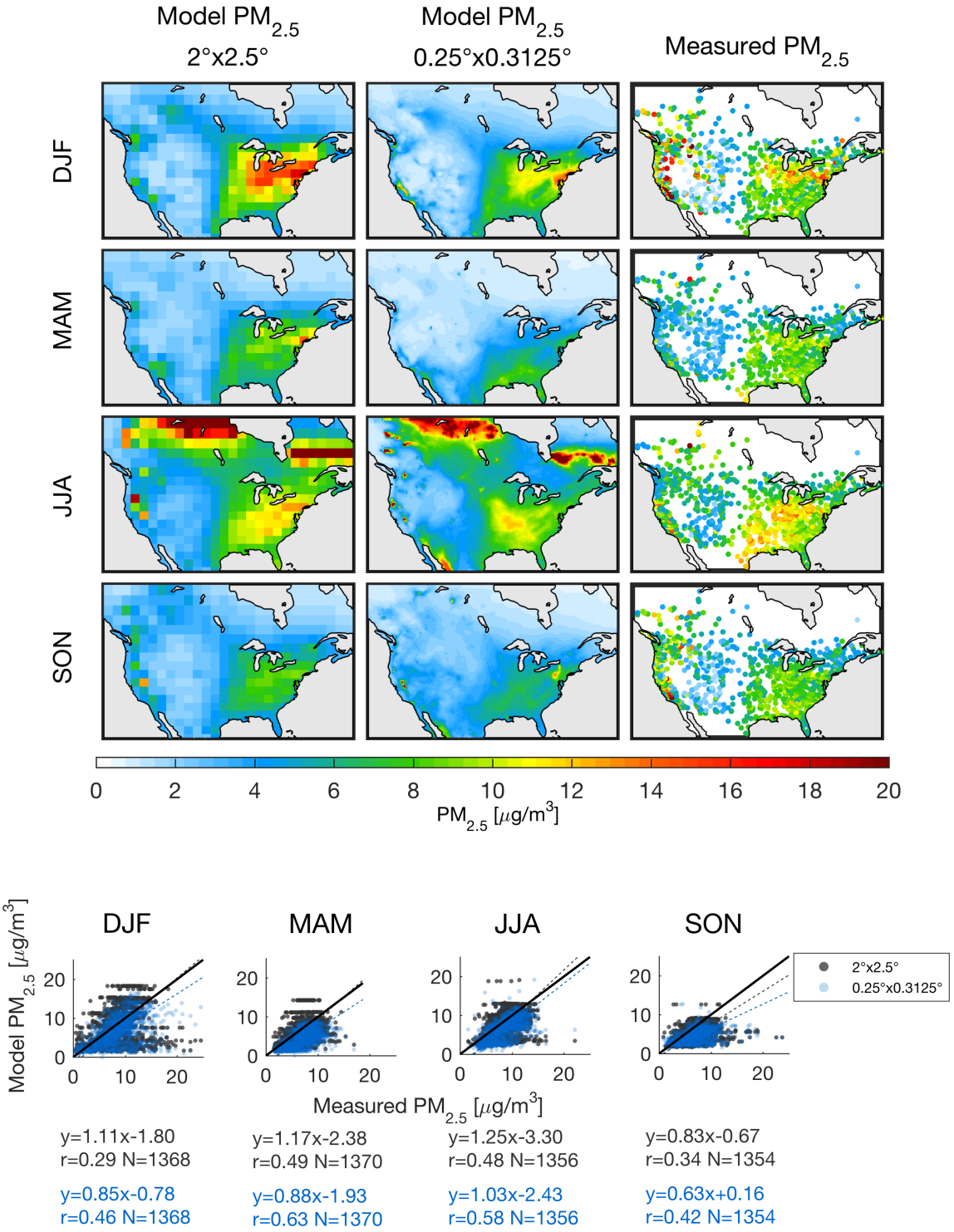

Figure 3.1 Seasonal mean (2013-2015) simulated $PM_{2.5}$ over North America at coarse (2° x 2.5°) and fine (0.25° x 0.3125°) model resolution. Comparison of model concentration versus in situ measurements at fine (blue) and coarse (grey) model resolution (bottom). Solid black line represents a 1:1 relationship between modeled and measured values. Dotted lines represent line of best fit for each simulation.

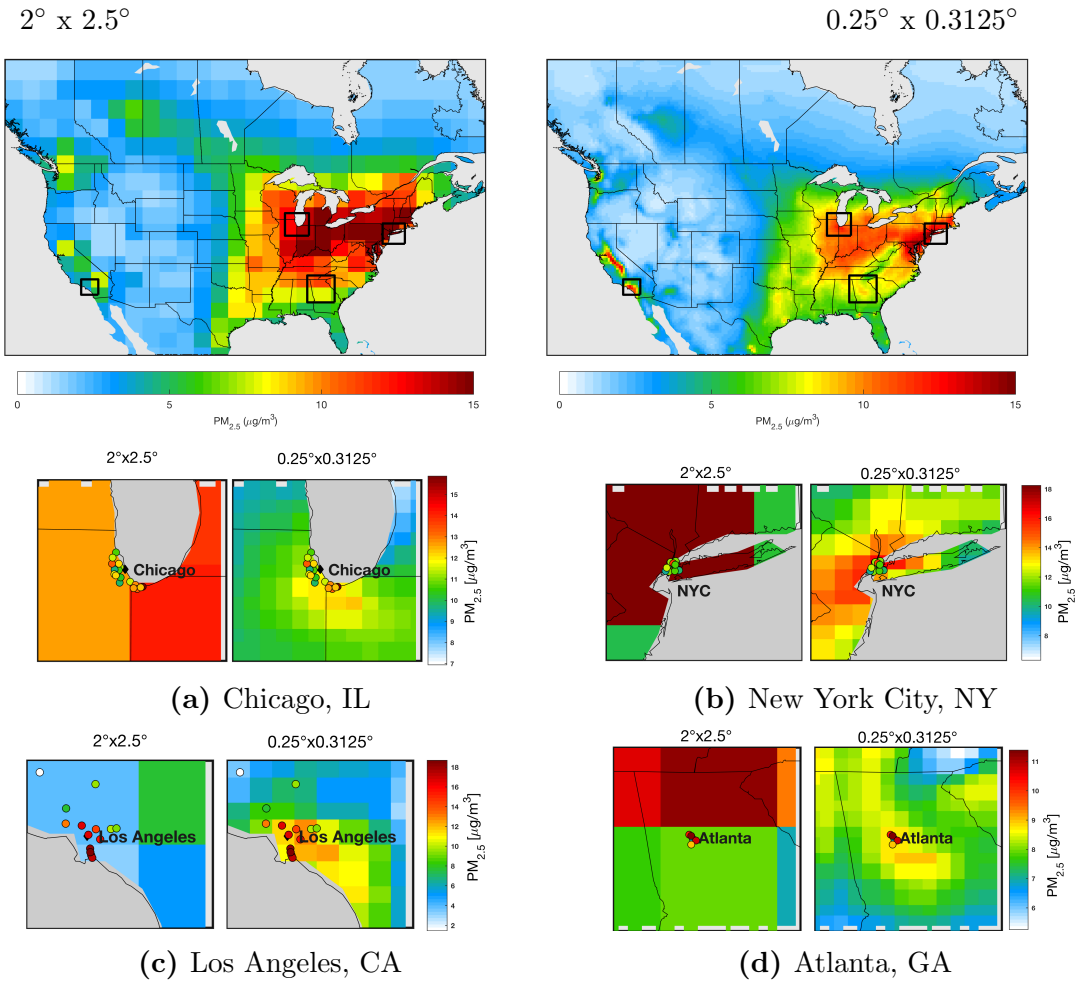

(a) Chicago, IL

(b) New York City, NY

(c) Los Angeles, CA

(d) Atlanta, GA

Figure 3.2 Annual mean (2013-2015) $PM_{2.5}$ over (a) Chicago, IL (b) New York City, NY (c) Los Angeles, CA and (d) Atlanta, GA at coarse (2° x 2.5°) and fine (0.25° x 0.3125°) model resolution. Black boxes on map (top) indicate the geographic boundaries of the regions shown below (a-d). Filled circles on regional plots indicate in situ measurements at that location.

The coarse and fine simulations differ primarily in their ability to resolve heterogeneity in surface $PM_{2.5}$ concentration. For example, the California Central Valley becomes apparent in the fine resolution simulation in winter and fall where it is not well represented in the coarse simulation. This geographic feature covers approximately 720 km in length while spanning 60 to 100 km in width; the width of the Valley is therefore a sub-grid scale feature in the coarse resolution simulation, but not in the fine resolution simulation. High $PM_{2.5}$ concentrations in this region are driven primarily by the local topography which limits ventilation and transport of pollutants in the region [*Chow et al.*, 2006]. This has the effect of enhancing simulated concentrations near the source of emissions. At coarse resolution, the consequence of this is a dilution of emitted aerosols throughout the encompassing grid cell, leading to the loss of the fine-scale valley feature and a relative enhancement in surrounding regions. Similar features include regions of biomass burning in the summer months seen along the entire west coast in the fine resolution simulation but nearly absent from the coarse resolution simulation.

The enhancement in the resolution of spatial features such as the California Valley is also observed in regions containing large urban centres, where population and emissions are dense, as shown in Figure 3.2. Ground-based measurements of $PM_{2.5}$ are shown in the filled circles. At the coarse resolution, the model is unable to resolve large urban areas and characterizes entire cities with a single value representing the entire grid box which may extend well beyond the city itself. The fine resolution simulation is able to resolve heterogeneities in surface $PM_{2.5}$, revealing elevated surface concentrations near urban centres which decreases with increasing distance from the city center.

Model Emissions

While emission inventories each have their own resolution (see Table 2.1) the total amount of aerosol emitted remains the same regardless of spatial and temporal model resolution. The key emission inventories used in this study have a finer resolution (i.e. 0.1° x 0.1°) than either of the conducted simulations (see Table 2.1). For each simulation, emissions from the 0.1° x 0.1° grid are added over the entire grid box area and the total value is taken to represent emissions for the entire box. This has the

effect of diluting emissions across an entire grid box area, an effect which deteriorates the accuracy of fine resolution emissions as grid size increases. Information on the peak density of emissions within a grid cell is often lost as a result.

The simulations in this study used the same emission inventories for the entire duration, with the exception of the anthropogenic emission inventory. NEI2011 was used from the beginning of the simulation (May 2013) to the end of 2013, EDGAR was used for 2014 onwards. Total monthly emissions over North America for August 2014 using each of these emission inventories are reported in Table 3.1 for comparison. The two emission inventories differ, with NEI2011 consistently reporting higher emissions for all species. NEI2011 emissions are based on EPA reported emissions for the year 2011 and then scaled to years between 2006 and 2013 using scale factors based on emission totals for each respective year relative to 2011. EDGAR works in a similar manner, with a base year of 2008 and scale factors available for the years 1970 to 2010. For years outside the available range GEOS-Chem continues to use the latest available year. The difference between inventories likely results from different assumptions and from the emissions being representative of different years, with higher emissions occurring in more recent years as represented by NEI2011. Section 3.6 explores the choice of anthropogenic emission inventory further.

Table 3.1 Monthly total emissions over North America for August 2014 using different anthropogenic emission inventories

Species	Run w/ EDGAR [Tg]	Run w/ NEI2011 [Tg]	NEI-EDG [%]
CO	10.45	10.57	1.1
NO	2.10	2.20	4.7
NH_3	0.66	0.69	5.2
SO_2	1.08	1.22	11.8
OC	0.32	0.33	4.7
BC	0.06	0.06	0.0

3.2 $PM_{2.5}$ Composition

While many health impact assessments focus on the adverse effects of $PM_{2.5}$ on human health some constituent species which make up $PM_{2.5}$ may be more detrimental to health than others. For example, studies conducted in multiple counties across Connecticut and Massachusetts found black carbon and road dust to be more harmful than other aerosols in $PM_{2.5}$ [*Mostofsky et al.*, 2012; *Bell et al.*, 2014]. Figure 3.3 shows the effect of resolution on modeled concentration of $PM_{2.5}$ constituent species SO4, NIT, NH4, secondary inorganic aerosols (SO4 + NIT + NH4), OM, BC, DST, and SALA. Figure 3.4 shows a scatter plot for each species illustrating the relationship between measured and modeled concentration. The relative contribution of each species to total $PM_{2.5}$ is shown in Figure 3.5. Differences in composition between resolutions is driven largely by differences in emission density.

3.2.1 Secondary Inorganics

Secondary inorganic aerosols, including SO_4^{2-}, NO_3^-, and NH_4^+, are formed from precursor gases such as SO_2, NOx, and NH_3, and are commonly associated with industrial emissions. $PM_{2.5}$ in North America is generally dominated by secondary inorganics and organic mass, together accounting for 60 to 90% of surface $PM_{2.5}$ concentration [*Ford and Heald*, 2013].

Measured and simulated SIA shown in Figure 3.3 reveal higher concentrations over the northeastern United States where industrial emissions are high. For all three secondary inorganic species, the coarse resolution simulation predicted greater peak surface concentration than fine resolution. Both coarse and fine resolution simulations achieve a strong correlation with measurements for SO_4^{2-} where $r = 0.88$ and 0.83, respectively (Figure 3.4). Simulated NO_3^- and NH_4^+ at fine resolution agreed with measurements more strongly than coarse resolution, with r values increasing from 0.38 to 0.50 for NO_3^- and from 0.62 to 0.67 for NH_4^+. For both species, the fine resolution simulation showed a near 1:1 relationship with measurements. Overall, the fine resolution simulation of SIA had a stronger agreement with measurements than the coarse resolution, with the correlation coefficient increasing from 0.57 to 0.66. The coarse resolution simulation had higher peak surface concentrations of SIA than

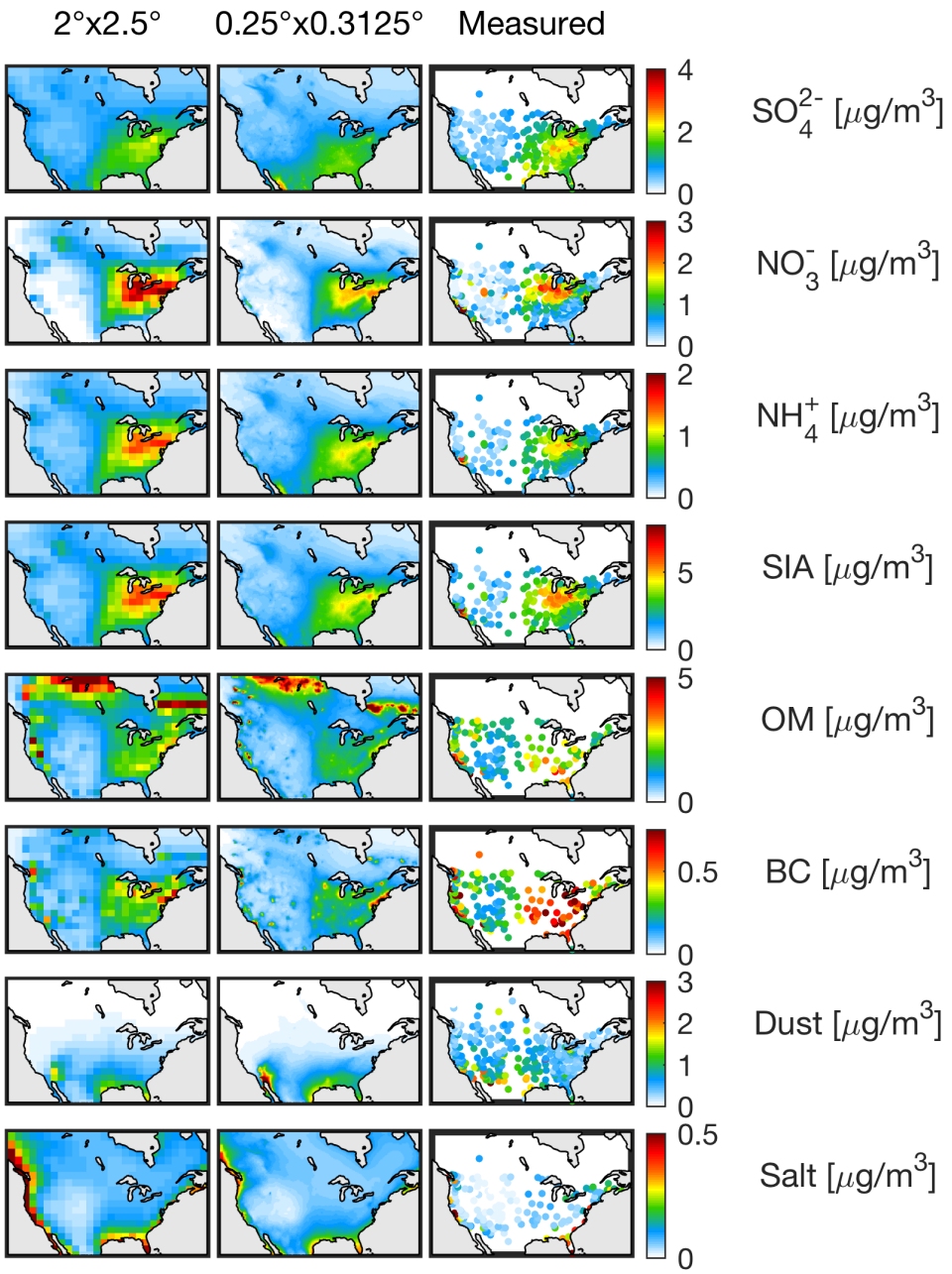

Figure 3.3 Annual mean (2013-2015) simulated concentrations of $PM_{2.5}$ constituent species at coarse (2° x 2.5°) and fine (0.25° x 0.3125°) resolution. Ground based measurements (right).

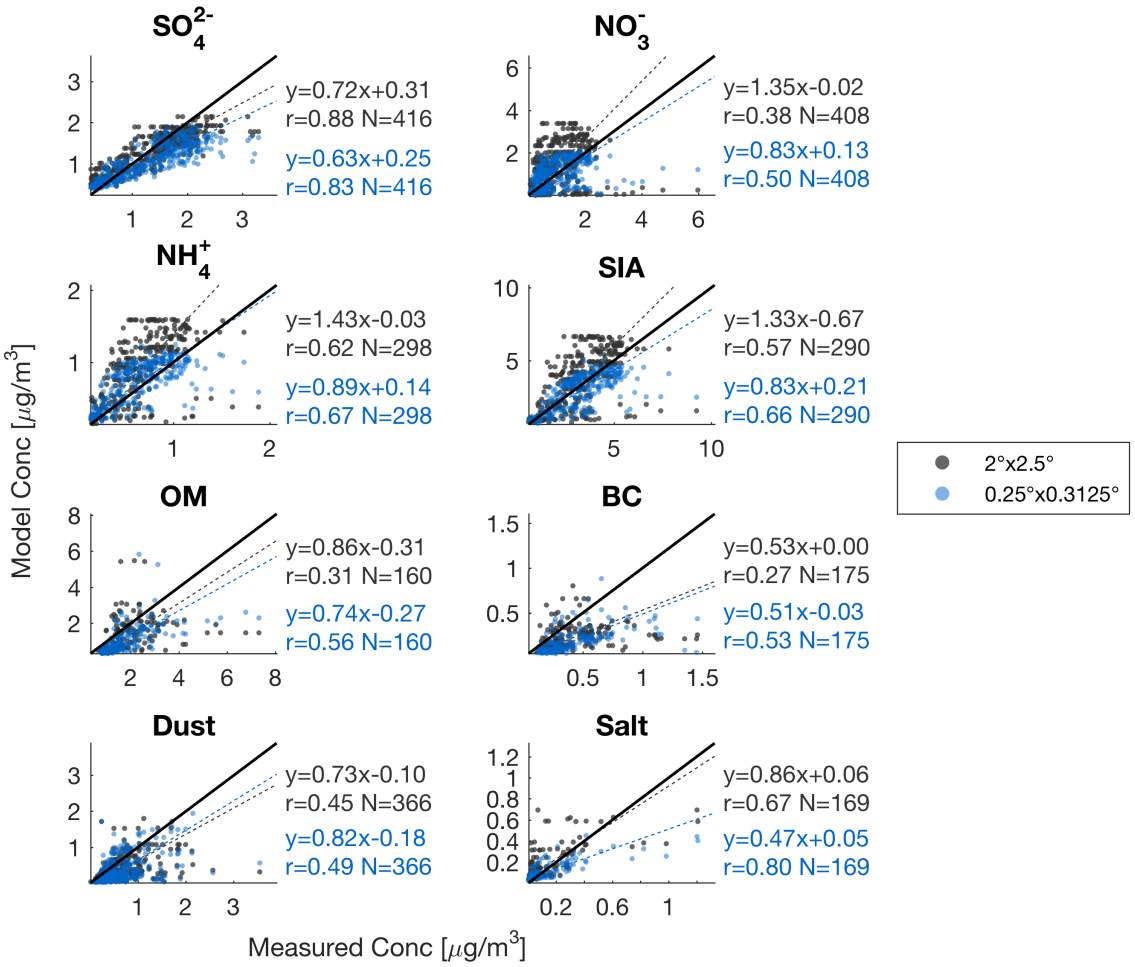

Figure 3.4 Comparison between model and in situ measurements for $PM_{2.5}$ species at fine (blue) and coarse (grey) model resolution. The solid black line represents a 1:1 relationship between modeled and measured values. Dotted lines represent lines of best fit for each simulation.

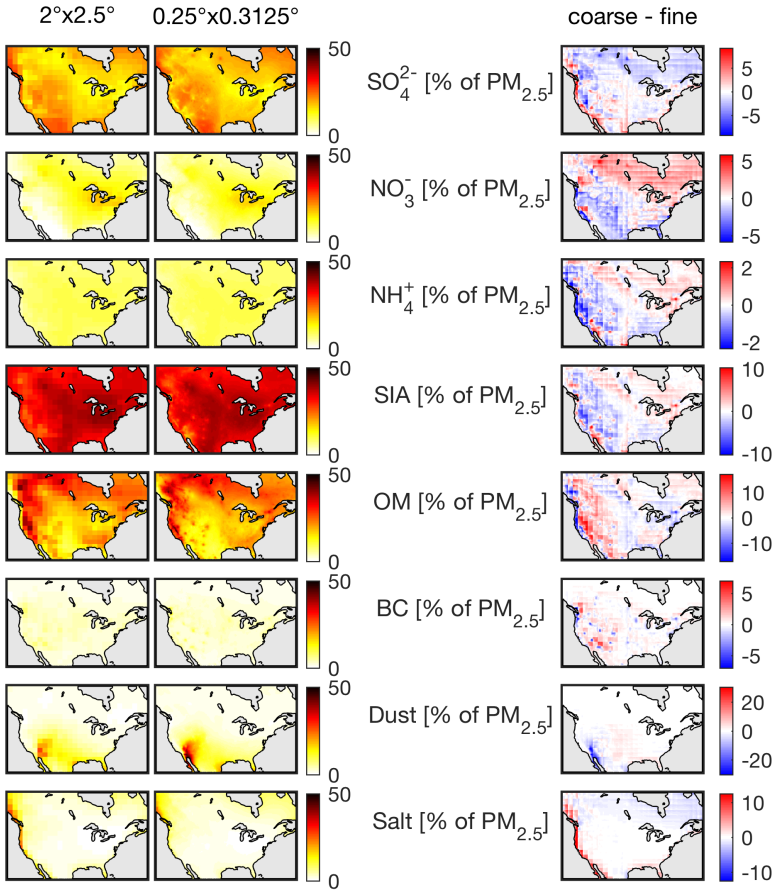

Figure 3.5 o
f each tracer to total surface $PM_{2.5}$ at coarse and fine model resolution]Annual mean (2013-2015) contribution [%] of each tracer to total surface $PM_{2.5}$ at coarse (left) and fine (right) model resolution.

the fine resolution simulation which accounts for much of the difference in total $PM_{2.5}$ as seen in Figure 3.1.

The relative contribution of SIA to total surface $PM_{2.5}$ (Figure 3.5) is greatest over northeastern North America and the continental interior. SIA contributes between 10% and 40% to total $PM_{2.5}$, with SO_4^{2-} being the dominant contributor to total SIA.

3.2.2 Organic Mass

Organic mass (OM) includes both primary (POA) and secondary (SOA) organic aerosols emitted from sources such as biomass burning, incomplete fossil fuel combustion, and biogenic emissions. Biomass burning and incomplete combustion are year-round sources, while biogenic emissions peak in spring and summer before dropping off in the fall months [*Kim et al.*, 2015]. Thus, the year-round source from fossil fuel burning dominates OM emissions.

Measured OM as shown in Figure 3.3 reflects this, with relatively high concentration in the eastern US where industrial emissions are greatest. Concentrations of OM are also high along the west coast where seasonal forest fires contribute to OM emissions. Simulations of OM capture this spatial trend, with a relative enhancement in surface OM in the east, and further enhancements in OM along the west coast. The fine resolution simulation is able to better resolve biomass burning regions which often occur on a sub-grid scale when using coarse resolution. Large regions of biomass burning in northern Canada are observed in both simulations. Measured OM concentrations are not available for these regions, illustrating the inability of ground-based measurements to fully describe surface $PM_{2.5}$ concentrations. Both coarse and fine resolution simulations achieve a near 1:1 relationship with measured values (slope = 0.86 and 0.74, respectively), with the fine resolution simulation having a stronger agreement with measurements ($r = 0.56$ compared to 0.31 for coarse).

The relative contribution of OM varies greatly across the continent, comprising as little as 1.4% to as much 47% of total $PM_{2.5}$. Across North America, the mean contribution of OM to total $PM_{2.5}$ is 18%.

3.2.3 Black Carbon

Black carbon is a highly absorbing component of $PM_{2.5}$ and therefore has a large contribution to AOD. BC measurements shown in Figure 3.3 reveal high BC concentrations in eastern North America and relatively low concentrations in the west. Several monitoring stations near the west coast report higher BC than in continental interior. BC emissions are dominated by fossil fuel burning, with biomass burning also contributing to total emissions [*Zhang et al.*, 2015]. Relatively high simulated BC concentration in the eastern US with small regions of enhanced concentration along the west coast is consistent with these emission sources. Figure 3.3 shows numerous small areas of enhanced BC at fine resolution which the coarse resolution simulation dilutes over a broad region or fails to capture entirely, indicating the strength of the fine resolution simulation at capturing fine scale emissions such as biomass burning events and sub-grid scale emissions.

3.2.4 Mineral Dust and Sea Salt

Fine dust aerosol, as seen in Figure 3.3, is most common in the southwestern United States due to the arid climate and around the Gulf coast due to the long-distance transport of dust from the Saharan desert in Africa. Coarse and fine resolution simulations perform similarly for mineral dust with an modest improvement in r from 0.45 to 0.49 when using fine resolution. Dust emission input data are at coarse resolution (4° x 5°), thus no dilution of dust emissions would occur at either resolution since both are more fine than emission resolution. The small change in slope and correlation coefficient between coarse and fine model resolution for dust illustrates the relatively small degree of change observed when emission density is consistent across model resolutions.

Measured sea salt aerosol concentrations are greatest in coastal regions, and relatively low in the continental interior. Both coarse and fine resolution simulations capture this spatial pattern well, with correlation coefficients of 0.67 and 0.80, respectively.

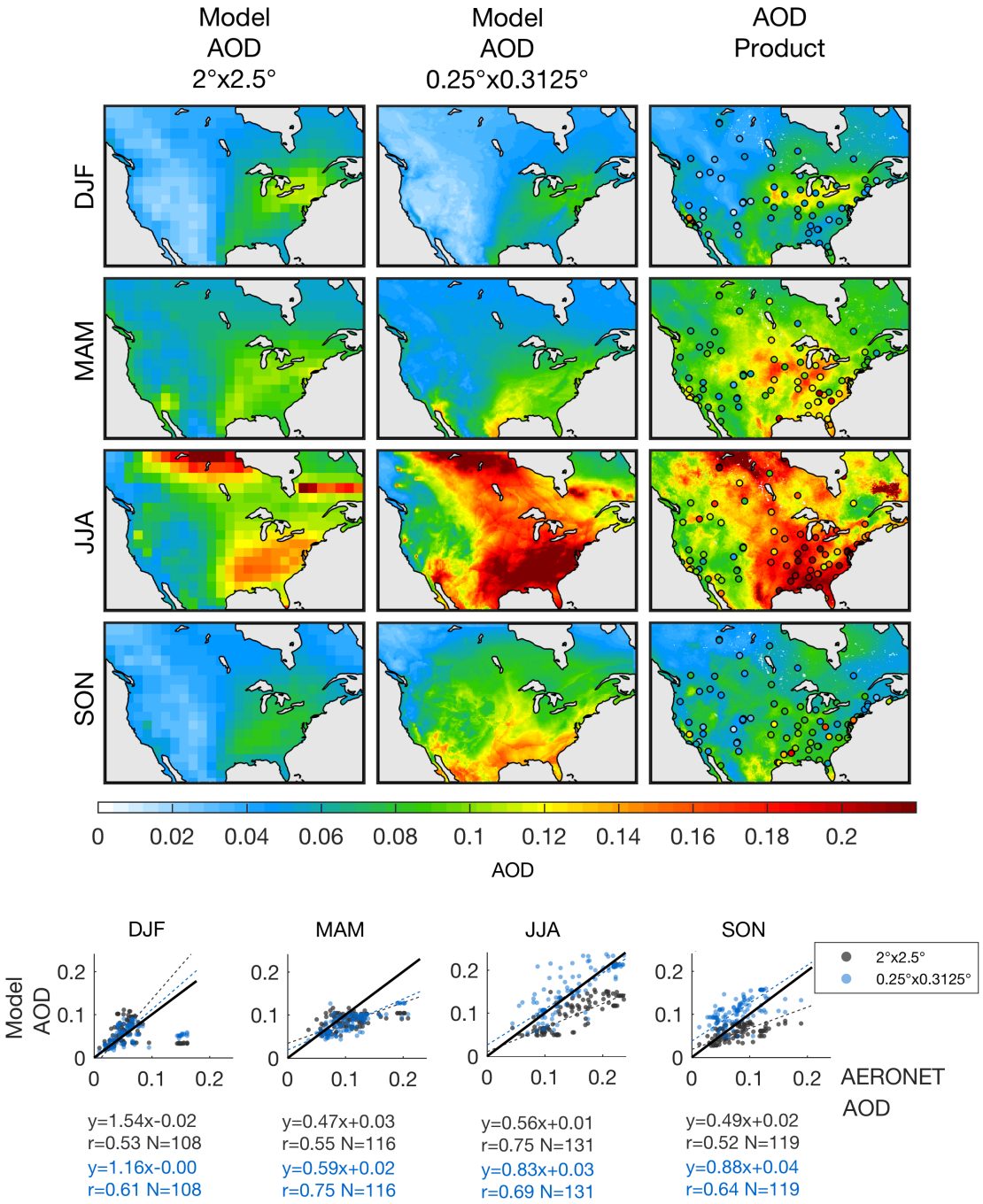

Figure 3.6 Seasonal mean (2013-2015) model AOD over North America at coarse (2° x 2.5°) and fine (0.25° x 0.3125°) model resolution and combined satellite AOD product created as described in *van Donkelaar et al.* [2016] and as outlined in Section 2.2. Filled circles on combined satellite maps show measured AERONET AOD. Comparison of model AOD versus AERONET measurements for fine (blue) and coarse (grey) model resolution (bottom). Solid black line in correlation plots represents a 1:1 relationship between modeled and measured values. Dotted lines represent best fit for each simulation.

3.3 Column AOD

Measured AOD shown in Figure 3.6 (right column) is represented by two sources: a combined satellite product as in *van Donkelaar et al.* [2016] and ground-based measurements from AERONET (filled circles). Seasonal variation in measured AOD is driven by aerosol sources, much as with $PM_{2.5}$, however seasonality in AOD is stronger than that in $PM_{2.5}$. This can be attributed to seasonal variation in mixed layer height. In the winter when the mixed layer is lower than in the summer, ventilation from the surface is reduced leading to enhancements in wintertime $PM_{2.5}$ at the surface, while the opposite is true in the summer [*Kim et al.*, 2015]. This seasonality is observed in measured AOD shown in Figure 3.6, where the greatest AOD is observed in summer and decreases in the cooler months. This is observed in both satellite and AERONET AOD.

As with $PM_{2.5}$, the highest aerosol loading occurs in areas with high population density and industrial activity and thus high emissions. Measured AOD shown in Figure 3.6 reflects this, with highest AOD occurring over the eastern United States. Simulated column AOD exhibits similar spatial patterns at coarse and fine resolution (Figure 3.6). The fine resolution simulation predicts greater AOD in summer and fall months than coarse resolution. The combined satellite product AOD is similar in magnitude to the fine resolution simulation AOD, with coarse resolution appearing to underestimate AOD in summer and fall. Comparison with AERONET measurements support this observation. The fine resolution simulation shows a slope of 0.83 and 0.88 for summer and fall, respectively, while the coarse resolution simulation shows a slope of 0.56 and 0.49.

Some fine scale spatial features emerge at 0.25° x 0.3125° resolution (i.e. California Central Valley in fall and biomass burning in the summer), as with model $PM_{2.5}$.

3.4 Surface-to-Column Ratio, η

The $PM_{2.5}$/AOD ratio is driven by $PM_{2.5}$ concentration at the surface, leading to the overall spatial pattern in η seen in Figure 3.7. As with $PM_{2.5}$, regions of high η occur over the eastern US in all seasons. Seasonal variation in η reveals a higher ratio in cooler months and a lower ratio in warmer months. This indicates that column AOD

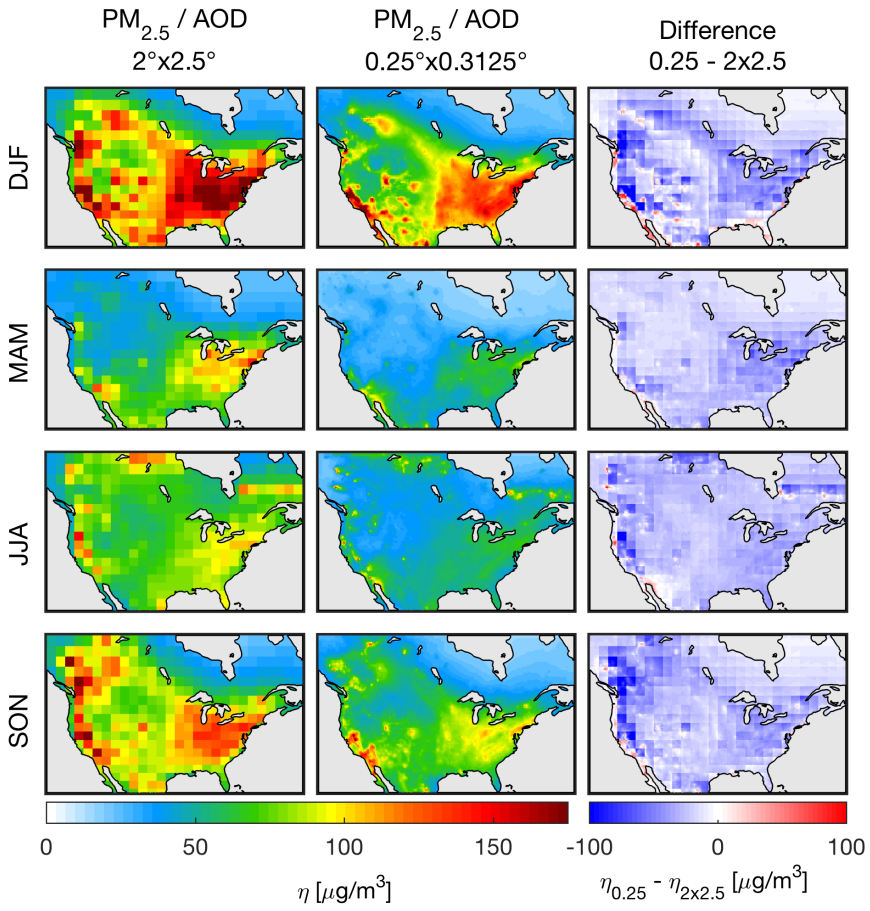

Figure 3.7 Seasonal mean (2013-2015) surface $PM_{2.5}$-to-column AOD ratio (η) over North America at coarse (2° x 2.5°) and fine (0.25° x 0.3125°) model resolution. Map of the difference between the two resolutions shown on right.

is relatively low compared to surface $PM_{2.5}$ in cooler months.

Recall Equation 1.6 from *Chu et al.* [2013] which expresses the aerosol surface-to-column ratio in terms of aerosol extinction cross-section at 550 nm wavelength per unit dry mass at surface ($\sigma_{\text{dry}}^{\text{ext}}$), aerosol mixing layer height (L_{mix}), and a hygroscopic growth factor (f_{RH}). Each of these factors can be independently examined to determine their relative influence on η.

$$\eta = \frac{\text{PM}_{2.5}}{\text{AOD}} = \frac{1}{L_{\text{mix}}\ [f(\text{RH})\ \sigma_{\text{dry}}^{\text{ext}}]_{\text{surface}}} \tag{3.1}$$

3.4.1 Aerosol Extinction Cross-section

The aerosol extinction cross-section ($\sigma_{\text{dry}}^{\text{ext}}$) describes how efficiently a given aerosol absorbs and scatters radiation, with higher $\sigma_{\text{dry}}^{\text{ext}}$ indicating greater extinction per unit mass of aerosol. The total $\sigma_{\text{dry}}^{\text{ext}}$ for $PM_{2.5}$ is a function of composition and $\sigma_{\text{dry}}^{\text{ext}}$ for each species. Figure 3.8 (from *Heald* [2010]) shows the extinction coefficient for each $PM_{2.5}$ constituent species as well as how this property varies with RH. While SIA and organic mass dominate surface $PM_{2.5}$ by mass (Figure 3.5), sulfate has a higher extinction efficiency than OM meaning sulfate has a greater contribution to AOD than OM per unit mass [*Kim et al.*, 2015]. Extinction efficiency is a property of aerosol species and does not vary between model resolutions. Differences in $\sigma_{\text{dry}}^{\text{ext}}$ between fine and coarse model resolution are therefore driven by estimated concentrations of each $PM_{2.5}$ constituent species and model RH (discussed further in Section 3.4.3 below).

Large aerosol extinction cross-section indicates high absorption and scattering of radiation by aerosols, leading to a high column AOD. Where column AOD is high, the ratio $PM_{2.5}$/AOD is relatively low. Figure 3.9 reveals this relationship, with higher $\sigma_{\text{dry}}^{\text{ext}}$ occurring in northern regions, leading to a low $PM_{2.5}$/AOD in the same area. Fine resolution $\sigma_{\text{dry}}^{\text{ext}}$ reveals fine scale spatial structure in $\sigma_{\text{dry}}^{\text{ext}}$ which is not captured in the coarse resolution simulation.

3.4.2 Mixing Layer Height

Mixing layer, or planetary boundary layer (PBL), height can impact surface concentrations of $PM_{2.5}$ by allowing or inhibiting vertical mixing. A low PBL causes an enhancement in surface concentration, leading to a relatively high amount of aerosol

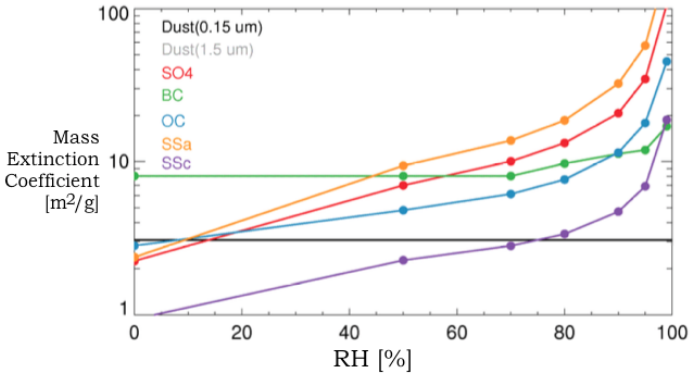

Figure 3.8 f
or $PM_{2.5}$ constituent species [*Heald*, 2010]]Changes in aerosol mass extinction coefficient [$m^2\,g^{-1}$] with relative humidity [%] for $PM_{2.5}$ constituent species. From *Heald* [2010].

at the surface and thus a high η. Conversely, a high PBL would lead to a relatively small η. Figure 3.9 illustrates the influence of model resolution on annual mean PBL height. PBL is highest over the southwestern US. $PM_{2.5}$/AOD is relatively low in this region illustrating the inverse relationship between PBL height and η. However, in northern regions where η is low, PBL is shown to be quite low also. In these regions, inhibited vertical mixing does not explain the spatial pattern in η.

3.4.3 Hygroscopic Growth Factor

The hygroscopic growth factor f_{RH} determines the growth of a given aerosol at the surface due to uptake of ambient moisture and is influenced by aerosol type and relative humidity. The growth factor is determined from the ratios of wet and dry effective radius ($r_{\mathrm{eff,i}}$) for each tracer i, as in Equation 3.2.

$$f_{\mathrm{RH}} = \frac{r_{\mathrm{eff},\mathbf{wet},\mathrm{i}}}{r_{\mathrm{eff},\mathbf{dry},\mathrm{i}}} \tag{3.2}$$

As with aerosol extinction cross-section, radiative properties are consistent between fine and coarse resolution simulations. That is, r_{eff} for a given species does not change regardless of model resolution. Variations in f_{RH} between model resolutions therefore result from differences in tracer concentrations (as discussed in Section 3.2) and differences in model RH.

Figure 3.9 (bottom) shows annual mean model surface RH at coarse and fine

resolution. Fine scale features, such as the Rocky Mountains, emerge at fine model resolution suggesting that differences between simulations at different resolutions are influenced by both emissions and meteorological input data.

Regions of high RH have a greater hygroscopic growth factor, and therefore more extinction by aerosols throughout the atmospheric column. This leads to an increase in AOD and therefore a decrease in η. This is observed in northern regions where RH is high and η is low.

Overall, the key variable influencing changes in η with changing model resolution follows from differences in simulated surface concentration of $PM_{2.5}$ constituent species. A more detailed representation of spatial gradients in surface concentration arises in the fine resolution simulation, where the coarse resolution simulation fails to capture such details due to coarse and often diluted emissions input data. Meteorological input data is also better resolved in the fine resolution simulation, leading to differences in aerosol growth due to uptake of ambient moisture. This affects aerosol extinction, and thus AOD which leads to differences in the surface-to-column ratio.

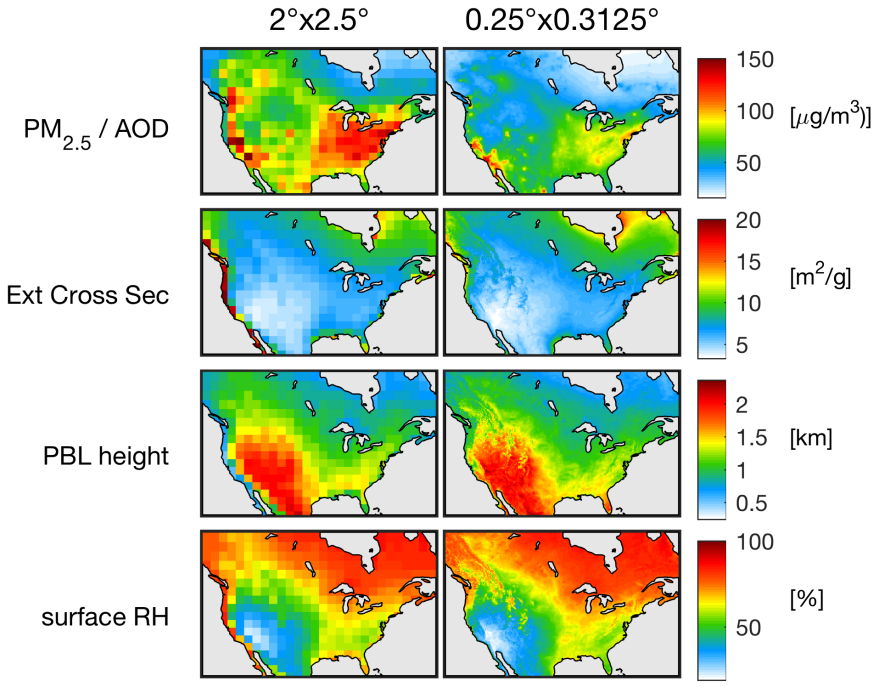

Figure 3.9 Annual mean surface $PM_{2.5}$-to-column AOD ratio (η), PBL height, and surface RH over North America at coarse (2° x 2.5°) and fine (0.25° x 0.3125°) model resolution.

3.5 Satellite-Model $PM_{2.5}$

Applying the $PM_{2.5}$/AOD ratio (η) from Section 3.4 to the combined satellite AOD product from *van Donkelaar et al.* [2016] yields the satellite-model estimated $PM_{2.5}$ shown in Figure 3.10.

Spatial and seasonal variation in $PM_{2.5}$ follow the same patterns as in model-only $PM_{2.5}$ as discussed in Section 3.1. Satellite-model $PM_{2.5}$ generated using fine model resolution η again captures spatial heterogeneities such as the California Central Valley in winter, a feature which appears more prominently in the satellite-model estimate than with the model alone. Interestingly, the coarse resolution satellite-model $PM_{2.5}$ reveals this feature as well, albeit not in as much detail. This illustrates a strength of incorporating satellite observations and model $PM_{2.5}$ to obtain more complete and accurate estimate of surface $PM_{2.5}$.

While incorporating the combined-satellite product with simulated aerosol concentrations does allow the coarse resolution simulation to resolve more spatial detail in surface $PM_{2.5}$ estimates, the fine resolution simulation continues to resolve features more precisely. Biomass burning emissions seen in the summer months provide a good example of this, where enhancements are observed at coarse resolution, but the spatial extent of these enhancements are more precisely defined at fine model resolution.

Table 3.2 further supports this, stating the slope and correlation coefficients for scatter plots comparing model and satellite-model $PM_{2.5}$ at coarse and fine resolution with ground-based measurements. For both fine and coarse simulations, incorporating the combined-satellite product led to as much as a 0.11 increase in explained variance. For all $PM_{2.5}$ estimates the strongest correlation with measurements occurred during the spring months and the poorest in the winter. Overall the fine resolution satellite-model estimates had the best agreement with measurements, with a near linear (1:1) slope and the highest correlation coefficients for each season.

3.6 Recommendations for Future Simulations

A wide range of potential settings for running GEOS-Chem exists. One-month sensitivity simulations for August 2014 at 0.25° x 0.3125° were conducted to determine

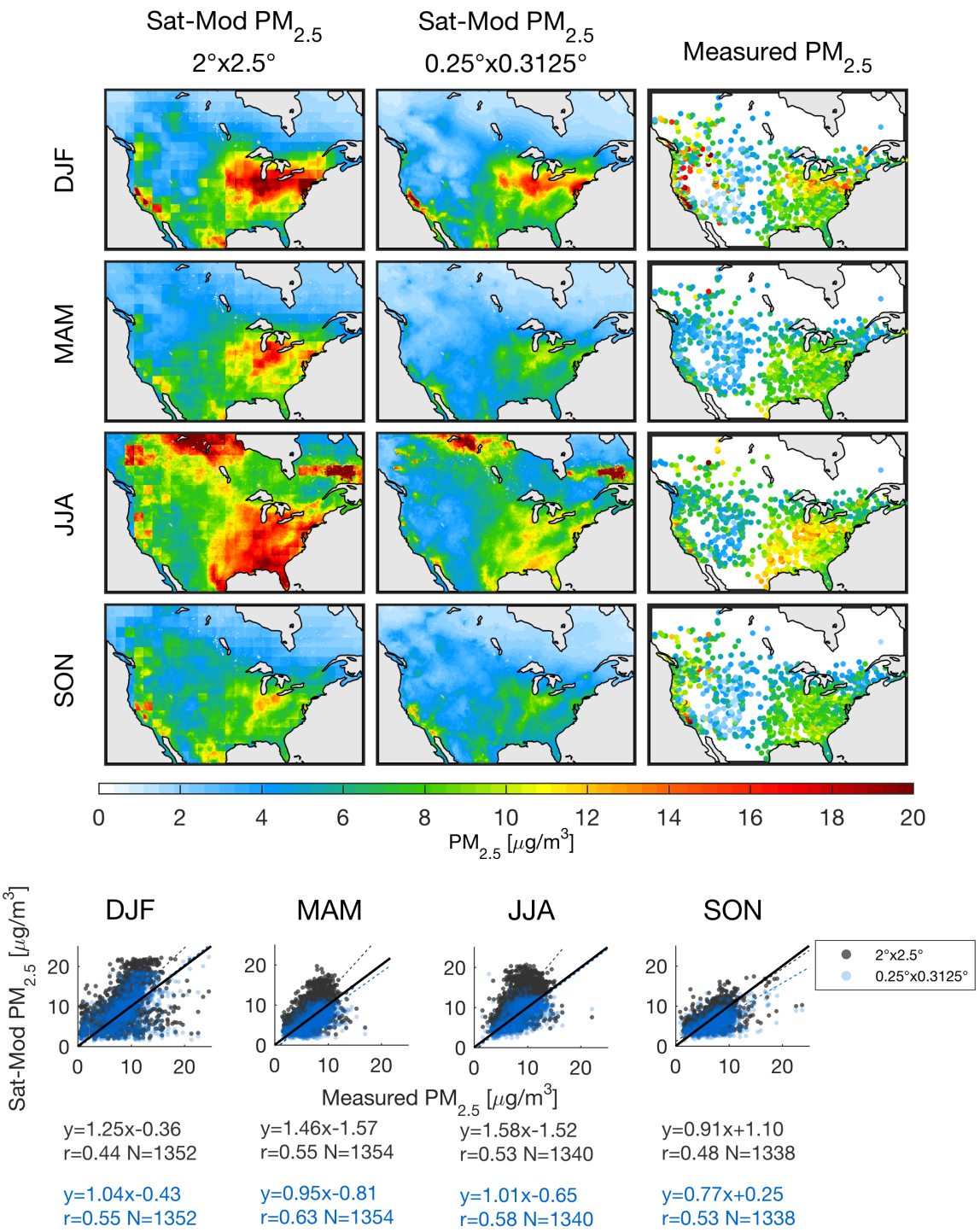

Figure 3.10 Seasonal mean (2013-2015) satellite-model $PM_{2.5}$ over North America at coarse (2° x 2.5°) and fine (0.25° x 0.3125°) model resolution. Comparison of satellite-model concentration from fine (blue) and coarse (grey) model simulations versus in situ measurements (bottom). Solid black line represents a 1:1 relationship between modeled and measured values. Dotted lines represent line of best fit for each simulation.

Table 3.2 Correlation coefficients for simulated vs. measured $PM_{2.5}$.

	MODEL				SAT-MOD			
	2° x 2.5°		0.25°		2° x 2.5°		0.25°	
Season	slope	r	slope	r	slope	r	slope	r
DJF	1.11	0.29	0.85	0.46	1.25	0.44	1.04	0.55
MAM	1.17	0.49	0.88	0.63	1.46	0.55	0.95	0.63
JJA	1.25	0.48	1.03	0.58	1.58	0.53	1.01	0.58
SON	0.83	0.34	0.63	0.42	0.91	0.48	0.77	0.53

which configuration yielded the best agreement with ground-based measurements.

3.6.1 Simulation Type: SOA vs. SVPOA

GEOS-Chem "full-chemistry" simulation with secondary organic aerosols (SOA) was used throughout this study. The SOA simulation treats primary organic aerosol (POA) as non-volatile, therefore POA is emitted, transported, and deposited in the particle phase. An alternative simulation type exists in which POA is treated as semi-volatile (SVPOA). In the SVPOA simulation, POA can partition between gas and aerosol phases. The effect of implementing SVPOA generally decreases simulated concentrations of organic aerosol, as a fraction of the emitted POA evaporates where it remained in the particle phase in the SOA simulation [*Pye and Seinfeld*, 2010].

This is consistent with the one-month test simulations shown in Figure 3.11 (a) and (b). The most notable difference between the SOA and SVPOA simulations is the reduction in $PM_{2.5}$ concentration in northern Canada. Recall from Figure 3.3 that elevated OM was responsible for high $PM_{2.5}$ concentration in this area. Allowing POA to enter the gas phase led to a decrease in particulate OM concentration. Enhancements in $PM_{2.5}$ over the eastern United States were also diminished in the SVPOA simulation relative to the SOA simulation, where OM was again a relatively large contributor to total $PM_{2.5}$ (Figure 3.5). Allowing a fraction of emitted POA to evaporate reduced surface $PM_{2.5}$ concentration to values which were more consistent with measurements. Comparison between model and measurements reveals an increase in model agreement from $r = 0.39$ (SOA) to 0.49 (SVPOA) and an improvement in slope from 2.27 to 1.24. The SVPOA simulation is therefore recommended

for future simulations.

3.6.2 Anthropogenic Emission Inventory: EDGAR vs. NEI2011

The default global anthropogenic emission inventory in GEOS-Chem is EDGAR. For simulations covering areas and time periods where regional emission inventories exist (e.g. NEI for the United States, CAC for Canada, and BRAVO for Mexico), regional emissions are given priority over the global inventory and thus overwrite EDGAR emissions. The most recent emissions inventory for the United States, NEI2011, covers the majority of North America (see Figure A.1) based on reported emissions for the year 2011. Annual scale factors are available for years ranging from 2006 to 2013. Beyond this time period, EDGAR is used.

For the one-month test simulations shown in Figure 3.11 several options were tested. The first used EDGAR, as in the rest of the work contained in this thesis (Figure 3.11 (b)). Using NEI2011 with a scale factor for the last available year of emissions (2013) was also tested (Figure 3.11 (c)). Finally, new scale factors were computed based on the 2014 National Emissions Inventory (NEI) Air Pollutant Emissions Trends Data [*US EPA*, 2016] (Figure 3.11 (d)). The currently available (2013) and newly computed scale factors are listed in Table 3.3.

Table 3.3 Annual scale factors (unitless) for calculating 2014 emissions based on reported emissions data from 2011

Species	Repeating 2013 Scale Factor	New 2014 Scale Factor
NO	0.887	0.855
CO	0.962	0.919
NH_3	0.998	0.996
VOC	0.971	0.944
SO_2	0.738	0.770
BC	0.991	0.989
OC	0.991	0.989

Of these three potential input data options for anthropogenic emissions, using NEI2011 with a scale factor based on 2014 emissions performed the strongest as compared to measured $PM_{2.5}$. The improvement between using NEI2011 with a 2013

versus 2014 scale factor was minimal, with the correlation coefficient increasing from 0.61 (2013 scale factor) to 0.63 (2014 scale factor). A much greater improvement was observed when compared with using the global EDGAR emission inventory, where r increased from 0.49 (EDGAR) to 0.63 (NEI2011 with 2014 scale factor). Based on these findings, future simulations should use the NEI2011 emissions inventory with updated scale factors based on the National Emissions Inventory (NEI) Air Pollutant Emissions Trends Data when simulating $PM_{2.5}$ over North America.

3.6.3 Biomass Burning Emission Inventory: With vs. Without Small Fires

The current default biomass burning inventory in GEOS-Chem is GFED4.1s, which includes burned area and emissions resulting from small fires. All simulations shown in Figure 3.11 use GFED4.1s with the exception of the bottom row which still uses GFED4.1 but with the emissions due to small fires removed. The effect of removing small fires can be seen in Figure 3.11 (e) where several small areas with elevated $PM_{2.5}$ are no longer present (i.e. northwestern Canada, western United States). Including emissions from small fires in the biomass burning inventory improves agreement with in situ measurements, with the r value increasing from 0.54 (without small fires) to 0.61 (with small fires). It is therefore recommended that future simulations continue to use GFED4.1s which includes biomass burning from small fires.

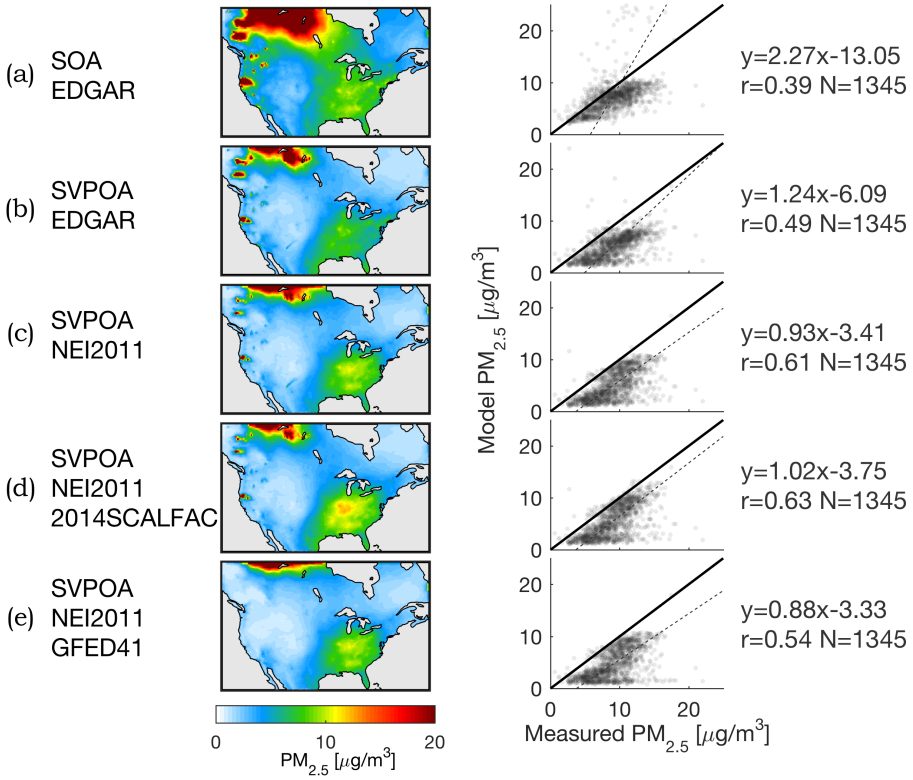

Figure 3.11 Comparison of 1-month GEOS-Chem test simulations for August 2014 using different simulation types and different emission inventories, as labelled in column on left. Agreement between model and in situ measurements is shown on right. The solid black line represents a 1:1 relationship between modeled and measured values. Dotted lines represent lines of best fit between modeled and measured values.

Chapter 4

Conclusions

4.1 Summary

Estimating $PM_{2.5}$ using a CTM with fine resolution (0.25° x 0.3125°) resulted in better estimates of surface $PM_{2.5}$ concentration than using coarse resolution (2° x 2.5°). Agreement with ground-based measurement of $PM_{2.5}$ showed an increase in explained variance ranging from 0.06 in fall to 0.16 in spring. The fine resolution simulation was able to resolve heterogeneities in surface $PM_{2.5}$, such as the California Central Valley in winter and biomass burning events in summer, which the coarse resolution was unable to resolve.

An examination of several urban centres emphasized the ability of the fine resolution simulation to resolve features in surface $PM_{2.5}$ which the coarse model could not. The ability to resolve large cities can aid in the accuracy of monitoring and mitigating adverse health impacts attributable to $PM_{2.5}$.

$PM_{2.5}$ constituent species also revealed surface features at fine resolution which were not present at coarse resolution. Black carbon provides a strong example with many localized enhancements in surface concentration in the eastern US in the fine resolution simulation compared to a broad enhancement over the entire region when using coarse resolution. This has important implications for health impact assessments, as BC may be one of the more detrimental aerosols to human health and therefore fine resolution estimates of its spatial distribution are highly valuable. The greatest improvement in surface estimates was for organic mass, for which agreement with measured concentration improved from $r = 0.31$ to $r = 0.56$ between fine and coarse resolution.

Simulated AOD captures seasonal variation well at both resolutions. Higher peak AOD is simulated at fine resolution than coarse.

Differences in $PM_{2.5}$/AOD (η) between model resolutions were driven by differences in surface $PM_{2.5}$ composition and the growth of constituent species due to RH. An exploration of aerosol extinction cross-section, PBL height, and surface relative

humidity revealed that differences in η were largely due to differences in simulated aerosol composition at the surface and throughout the column. Differences in composition between resolutions was largely influenced by emission density.

Satellite-model estimates of $PM_{2.5}$ were produced from simulated $PM_{2.5}$, AOD, and the combined satellite product. The incorporation of satellite observations improved surface $PM_{2.5}$ estimates over using the model only. The strongest estimates of surface $PM_{2.5}$ were generated when using the fine model resolution combined with satellite data.

Future simulations should consider the SVPOA simulation which allows POA to enter the gas phase, NEI2011 regional emissions for anthropogenic emissions over North America, and should continue to include the contribution of small fires in the GFED4.1s biomass burning emissions inventory.

4.2 Closing Remarks

Simulating $PM_{2.5}$ surface concentrations at fine scale resolution improves estimates over coarse resolution. Incorporating satellite-derived observations further strengthens the agreement between surface $PM_{2.5}$ estimates and ground-based measurements. Results of these simulations can provide health impact assessments with more detailed information around urban centres to determine the effects and mitigate levels of ambient air pollution in these densely populated regions. Regions where extensive ground-based monitoring is not feasible can benefit from satellite-model estimate $PM_{2.5}$.

Bibliography

Arunachalam, S., B. Wang, N. Davis, B. H. Baek, and J. I. Levy, Effect of chemistry-transport model scale and resolution on population exposure to PM2.5 from aircraft emissions during landing and takeoff, *Atmospheric Environment*, *45*(19), 3294–3300, doi:10.1016/j.atmosenv.2011.03.029, 2011.

Bell, M. L., K. Ebisu, B. P. Leaderer, J. F. Gent, H. J. Lee, P. Koutrakis, Y. Wang, F. Dominici, and R. D. Peng, Associations of PM2.5 constituents and sources with hospital admissions: Analysis of four counties in connecticut and Massachusetts (USA) for persons over 65 years of age, *Environmental Health Perspectives*, *122*(2), 138–144, doi:10.1289/ehp.1306656, 2014.

Benkovitz, C. M., M. T. Scholtz, J. Pacyna, L. Tarrasón, J. Dignon, E. C. Voldner, P. a. Spiro, J. a. Logan, and T. E. Graedel, Global gridded inventories of anthropogenic emissions of sulfur and nitrogen, *Journal of Geophysical Research*, *101*(D22), 29,239, doi:10.1029/96JD00126, 1996.

Bey, I., et al., Global modeling of tropospheric chemistry with assimilated meteorology: Model description and evaluation, *Journal of Geophysical Research*, *106*(D19), 23,073–23,095, doi:10.1029/2001JD000807, 2001.

Boucher, O., et al., Clouds and Aerosols, in *Climate Change 2013: The Physical Science Basis. Contribtuion of Working Group I to the Fifth Assessment Report of the Intergovernmental Panel on Climate Change*, edited by T. Stocker, D. Qin, G.-K. Plattner, M. Tignor, S. Allen, J. Boschung, A. Nauels, Y. Xia, V. Bex, and P. Midgley, chap. Clouds and, pp. 571–657, Cambridge University Press, Cambridge, United Kingdom and New York, NY, USA, 2013.

Canadian Council of Ministers of the Environment, Canada-Wide Standards for Particulate Matter and Ozone: 2012 Final Report, *Tech. rep.*, Canadian Council of Ministers of the Environment, 2014.

Chow, J. C., and J. G. Watson, Guideline on Speciated Particulate Monitoring, *Tech. rep.*, Desert Research Institute, Reno, NV, 1998.

Chow, J. C., L. W. A. Chen, J. G. Watson, D. H. Lowenthal, K. a. Magliano, K. Turkiewicz, and D. E. Lehrman, PM2.5 chemical composition and spatiotemporal variability during the Californian Regional PM10/PM2.5 Air Quality Study (CRPAQS), *Journal of Geophysical Research: Atmospheres*, *111*(10), doi:10.1029/2005JD006457, 2006.

Chu, D. A., T. C. Tsai, J. P. Chen, S. C. Chang, Y. J. Jeng, W. L. Chiang, and N. H. Lin, Interpreting aerosol lidar profiles to better estimate surface PM2.5 for columnar AOD measurements, *Atmospheric Environment*, *79*, 172–187, doi:10.1016/j.atmosenv.2013.06.031, 2013.

Correia, A., C. Pope III, D. W. Dockery, Y. Wang, M. Ezzati, and F. Dominici, The effect of air pollution control on life expectancy in the United States: an analysis of 545 US counties for the period 2000 to 2007, *Epidemiology*, *24*(1), 23–31, doi: 10.1097/EDE.0b013e3182770237.The, 2013.

Crouse, D. L., et al., Risk of nonaccidental and cardiovascular mortality in relation to long-term exposure to low concentrations of fine particulate matter: A canadian national-level cohort study, *Environmental Health Perspectives*, *120*(5), 708–714, doi:10.1289/ehp.1104049, 2012.

Cuvelier, C., et al., ScaleDep: Performance of European chemistry-transport models as function of horizontal spatial resolution, *Tech. rep.*, Norwegian Meteorological Institute, 2013.

Diehl, T., A. Heil, M. Chin, X. Pan, D. Streets, M. Schultz, and S. Kinne, Anthropogenic, biomass burning, and volcanic emissions of black carbon, organic carbon, and SO2 from 1980 to 2010 for hindcast model experiments, *Atmospheric Chemistry and Physics Discussions*, *12*, 24,895–24,954, doi:10.5194/acpd-12-24895-2012, 2012.

Environment and Climate Change Canada, Pollution and Waste - Tracking Pollution in Canada, Retrieved from http://www.ec.gc.ca/inrp-npri/, 2016a.

Environment and Climate Change Canada, National Air Pollution Surveillance Program, Retrieved from http://www.ec.gc.ca/rnspa-naps/, 2016b.

Eyring, V., H. W. Köhler, J. van Aardenne, and A. Lauer, Emissions from international shipping: 1. The last 50 years, *J. Geophys. Res.*, *110*(D17), D17,305, doi:10.1029/2004jd005619, 2005.

Fairlie, D. T., D. J. Jacob, and R. J. Park, The impact of transpacific transport of mineral dust in the United States, *Atmospheric Environment*, *41*(6), 1251–1266, doi:10.1016/j.atmosenv.2006.09.048, 2007.

Fairlie, T. D., D. J. Jacob, J. E. Dibb, B. Alexander, M. A. Avery, A. Van Donkelaar, and L. Zhang, Impact of mineral dust on nitrate, sulfate, and ozone in transpacific Asian pollution plumes, *Atmospheric Chemistry and Physics*, *10*(8), 3999–4012, doi:10.5194/acp-10-3999-2010, 2010.

Ford, B., and C. L. Heald, Aerosol loading in the Southeastern United States: Reconciling surface and satellite observations, *Atmospheric Chemistry and Physics*, *13*(18), 9269–9283, doi:10.5194/acp-13-9269-2013, 2013.

Fountoukis, C., D. Koraj, H. A. C. D. V. D. Gon, P. E. Charalampidis, C. Pilinis, and S. N. Pandis, Impact of grid resolution on the predicted fi ne PM by a regional 3-D chemical transport model, *Atmospheric Environment*, *68*, 24–32, doi:10.1016/j.atmosenv.2012.11.008, 2013.

GEOS-Chem Support Team, Aerosol Optical Properties, Retrieved from http://wiki.seas.harvard.edu/geos-chem/index.php/Aerosol_optical_properties, 2014.

Giglio, L., and J. T. Randerson, The Version 4 Global Fire Emissions Database (GFED4) Burned Area Component, *Tech. rep.*, University of Maryland, 2013.

Giglio, L., J. T. Randerson, and G. R. Van Der Werf, Analysis of daily, monthly, and annual burned area using the fourth-generation global fire emissions database (GFED4), *Journal of Geophysical Research: Biogeosciences*, *118*(1), 317–328, doi: 10.1002/jgrg.20042, 2013.

Goldstein, A. H., C. D. Koven, C. L. Heald, and I. Y. Fung, Biogenic carbon and anthropogenic pollutants combine to form a cooling haze over the southeastern United States., *Proceedings of the National Academy of Science*, *106*(22), 8835–8840, doi:10.1073/pnas.0904128106, 2009.

Guenther, A. B., X. Jiang, C. L. Heald, T. Sakulyanontvittaya, T. Duhl, L. K. Emmons, and X. Wang, The model of emissions of gases and aerosols from nature version 2.1 (MEGAN2.1): An extended and updated framework for modeling biogenic emissions, *Geoscientific Model Development*, *5*(6), 1471–1492, doi: 10.5194/gmd-5-1471-2012, 2012.

Harvard Atmospheric Chemistry and Modeling Group, Particulate matter in GEOS-Chem, Retrieved from http://wiki.seas.harvard.edu/geos-chem/index.php/Particulate_matter_in_GEOS-Chem, 2016.

Heald, C. L., GEOS-Chem Aerosol Optics, Retrieved from http://www.atmos.colostate.edu/~heald/docs/GEOS_Chem_optics_description.pdf, 2010.

Heald, C. L., et al., Atmospheric ammonia and particulate inorganic nitrogen over the United States, *Atmospheric Chemistry and Physics*, *12*, 10,295–10,312, doi: 10.5194/acp-12-10295-2012, 2012.

Hoff, R. M., and S. A. Christopher, Remote Sensing of Particulate Pollution from Space: Have We Reached the Promised Land?, *Journal of the Air & Waste Management Association*, *59*(6), 645–675, doi:10.3155/1047-3289.59.6.645, 2009.

Hsu, N. C., S. C. Tsay, M. D. King, and J. R. Herman, Aerosol properties over bright-reflecting source regions, *IEEE Transactions on Geoscience and Remote Sensing*, *42*(3), 557–569, doi:10.1109/TGRS.2004.824067, 2004.

Hudman, R. C., N. E. Moore, A. K. Mebust, R. V. Martin, A. R. Russell, L. C. Valin, and R. C. Cohen, Steps towards a mechanistic model of global soil nitric oxide emissions: Implementation and space based-constraints, *Atmospheric Chemistry and Physics*, *12*(16), 7779–7795, doi:10.5194/acp-12-7779-2012, 2012.

Jacob, D. J., Chapter 3: Simple Models, in *Introduction to Atmospheric Chemistry*, pp. 22–34, Princeton University Press, Princeton, NJ, 1999.

Keller, C. a., M. S. Long, R. M. Yantosca, a. M. Da Silva, S. Pawson, and D. J. Jacob, HEMCO v1.0: a versatile, ESMF-compliant component for calculating emissions in atmospheric models, *Geoscientific Model Development*, *7*, 1409–1417, doi:10.5194/gmd-7-1409-2014, 2014.

Kim, P. S., et al., Source, seasonality, and trends of Southeast US aerosol: an integrated analysis of surface, aircraft, and satellite observations with the GEOS-Chem chemical transport model, *Atmospheric Chemistry and Physics*, *15*(18), 10,411–10,433, doi:10.5194/acp-15-10411-2015, 2015.

Kuhns, H., M. Green, and V. Etyemezian, Big Bend Regional Aerosol and Visibility Observational (BRAVO) Study Emissions Inventory, technical report prepared for the BRAVO Steering Committee, *Tech. rep.*, Desert Research Institute, 2001.

Lee, S. J., M. L. Serre, A. van Donkelaar, R. V. Martin, R. T. Burnett, and M. Jerrett, Comparison of geostatistical interpolation and remote sensing techniques for estimating long-term exposure to ambient PM2.5 concentrations across the continental United States, *Environmental Health Perspectives*, *120*(12), 1727–1732, doi:10.1289/ehp.1205006, 2012.

Levy, R. C., L. A. Remer, R. G. Kleidman, S. Mattoo, C. Ichoku, R. Kahn, and T. F. Eck, Global evaluation of the Collection 5 MODIS dark-target aerosol products over land, *Atmospheric Chemistry and Physics*, *10*(21), 10,399–10,420, doi:10.5194/acp-10-10399-2010, 2010.

Levy, R. C., S. Mattoo, L. a. Munchak, L. a. Remer, a. M. Sayer, F. Patadia, and N. C. Hsu, The Collection 6 MODIS aerosol products over land and ocean, *Atmospheric Measurement Techniques*, *6*, 2989–3034, doi:10.5194/amt-6-2989-2013, 2013.

Li, Y., D. K. Henze, D. Jack, and P. L. Kinney, The influence of air quality model resolution on health impact assessment for fine particulate matter and its components, *Air Quality, Atmosphere & Health*, doi:10.1007/s11869-015-0321-z, 2015.

Lim, S. S., et al., A comparative risk assessment of burden of disease and injury attributable to 67 risk factors and risk factor clusters in 21 regions, 1990-2010: A systematic analysis for the Global Burden of Disease Study 2010, *The Lancet*, *380*, 2224–2260, doi:10.1016/S0140-6736(12)61766-8, 2012.

Loomis, D., W. Huang, and G. Chen, The International Agency for Research on Cancer (IARC) evaluation of the carcinogenicity of outdoor air pollution: Focus on China, *Chinese Journal of Cancer*, *33*(4), 189–196, doi:10.5732/cjc.014.10028, 2014.

Lyapustin, A., Y. Wang, I. Laszlo, R. Kahn, S. Korkin, L. Remer, R. Levy, and J. S. Reid, Multiangle implementation of atmospheric correction (MAIAC): 2. Aerosol algorithm, *Journal of Geophysical Research Atmospheres*, *116*(3), 1–15, doi:10.1029/2010JD014986, 2011.

Malm, W. C., J. F. Sisler, D. Huffman, R. A. Eldred, and T. A. Cahill, Spatial and seasonal trends in particle concentration and optical extinction in the United States, *Journal of Geophysical Research*, *99*(D1), 1347–1370, 1994.

Martonchik, J. V., D. J. Diner, R. A. Kahn, T. P. Ackerman, M. M. Verstraete, B. Pinty, and H. R. Gordon, Techniques for the retrieval of aerosol properties over land and ocean using multiangle imaging, *IEEE Transactions on Geoscience and Remote Sensing*, *36*(4), 1212–1227, doi:10.1109/36.701027, 1998.

Mostofsky, E., J. Schwartz, B. A. Coull, P. Koutrakis, G. A. Wellenius, H. H. Suh, D. R. Gold, and M. A. Mittleman, Modeling the association between particle constituents of air pollution and health outcomes, *American Journal of Epidemiology*, *176*(4), 317–326, doi:10.1093/aje/kws018, 2012.

Muntean, M., G. Janssens-Maenhout, S. Song, N. E. Selin, J. G. J. Olivier, D. Guizzardi, R. Maas, and F. Dentener, Trend analysis from 1970 to 2008 and model evaluation of EDGARv4 global gridded anthropogenic mercury emissions, *Science of the Total Environment*, *494-495*, 337–350, doi:10.1016/j.scitotenv.2014.06.014, 2014.

Murray, L. T., D. J. Jacob, J. A. Logan, R. C. Hudman, and W. J. Koshak, Optimized regional and interannual variability of lightning in a global chemical transport model constrained by LIS/OTD satellite data, *Journal of Geophysical Research Atmospheres*, *117*(20), 1–14, doi:10.1029/2012JD017934, 2012.

NASA Goddard Space Flight Center; MODIS, MODIS Web, Retrieved from http://modis.gsfc.nasa.gov/, 2016.

NASA Goddard Space Flight Center; SeaWiFS, SeaWiFS Project - Spacecraft and Sensor Overview, Retrieved from http://oceancolor.gsfc.nasa.gov/SeaWiFS, 2016.

NASA Jet Propulsion Laboratory; MISR, MISR: Home Page, Retrieved from http://www-misr.jpl.nasa.gov/, 2016.

Philip, S., et al., Global Chemical Composition of Ambient Fine Particulate Matter for Exposure Assessment: Supporting Information, *Environmental Science and Technology*, *48*, 13,060–13,068, 2014a.

Philip, S., et al., Spatially and seasonally resolved estimate of the ratio of organic mass to organic carbon, *Atmospheric Environment*, *87*, 34–40, doi:10.1016/j.atmosenv.2013.11.065, 2014b.

Pinto, J. P., A. S. Lefohn, and D. S. Shadwick, Spatial Variability of PM 2.5 in Urban Areas in the United States, *Journal of the Air & Waste Management Association*, *54*(4), 440–449, doi:10.1080/10473289.2004.10470919, 2004.

Pitchford, M., W. Maim, B. Schichtel, N. Kumar, D. Lowenthal, and J. Hand, Revised algorithm for estimating light extinction from IMPROVE particle speciation data, *Journal of the Air & Waste Management Association*, *57*, 1326–1336, doi:10.3155/1047-3289.57.11.1326, 2007.

Pope III, C. A., M. Ezzati, and D. W. Dockery, Fine particulate air pollution and US county life expectancies, *New England Journal of Medicine*, *360*(4), 376–386, doi:10.1056/NEJMsa0805646.Fine, 2009.

Punger, E. M., and J. J. West, The effect of grid resolution on estimates of the burden of ozone and fine particulate matter on premature mortality in the USA, *Air Quality, Atmosphere and Health*, *6*(3), 563–573, doi:10.1007/s11869-013-0197-8, 2013.

Pye, H. O. T., and J. H. Seinfeld, A global perspective on aerosol from low-volatility organic compounds, *Atmospheric Chemistry and Physics*, *10*(9), 4377–4401, doi:10.5194/acp-10-4377-2010, 2010.

Reinhart, W., and D. Millet, Implementation of the RETRO Anthropogenic Emission Inventory into the GEOS-Chem Model, *Tech. Rep. Table 1*, University of Minesota, 2011.

Remer, L. A., et al., Global aerosol climatology from the MODIS satellite sensors, *Journal of Geophysical Research Atmospheres*, *113*(14), 1–18, doi:10.1029/2007JD009661, 2008.

Savtchenko, A., D. Ouzounov, S. Ahmad, J. Acker, G. Leptoukh, J. Koziana, and D. Nickless, Terra and Aqua MODIS products available from NASA GES DAAC, *Advances in Space Research*, *34*(4), 710–714, doi:10.1016/j.asr.2004.03.012, 2004.

Schultz, M. G., A. Heil, J. J. Hoelzemann, A. Spessa, K. Thonicke, J. G. Goldammer, A. C. Held, J. M. C. Pereira, and M. van Het Bolscher, Global wildland fire emissions from 1960 to 2000, *Global Biogeochemical Cycles*, *22*(2), 1–17, doi:10.1029/2007GB003031, 2008.

Shindell, D., et al., Chapter 2: Atmosphere, in *Geo 5 - Unep*, edited by B. Ullstein, H. de Mattos, C. Hawkins, C. P. McMullen, J. Jabbour, and J. Scharlemann, chap. Atmosphere, pp. 31–64, Progress Press Ltd., Malta, 2012.

Stanek, L. W., et al., Integrated Science Assessment for Particulate Matter, *Tech. Rep. December 2009*, U.S. Environmental Protection Agency, 2009.

Stettler, M. E. J., S. Eastham, and S. R. H. Barrett, Air quality and public health impacts of UK airports. Part I: Emissions, *Atmospheric Environment*, *45*(31), 5415–5424, doi:10.1016/j.atmosenv.2011.07.012, 2011.

Thompson, T. M., R. K. Saari, and N. E. Selin, Air quality resolution for health impact assessment: Influence of regional characteristics, *Atmospheric Chemistry and Physics*, *14*(2), 969–978, doi:10.5194/acp-14-969-2014, 2014.

US EPA, Air Pollutant Emissions Trends Data, Retrieved from https://www.epa.gov/air-emissions-inventories/air-pollutant-emissions-trends-data, 2016.

US EPA Office of Air Quality Planning and Standards, Clean Air Status and Trends Network, Retrieved from https://www.epa.gov/castnet, 2016a.

US EPA Office of Air Quality Planning and Standards, AirData website Home page, Retrieved from https://www.epa.gov/outdoor-air-quality-data/, 2016b.

US EPA Office of Air Quality Planning and Standards, NAAQS Table, Retrieved from https://www.epa.gov/criteria-air-pollutants/naaqs-table, 2016c.

US EPA Office of Air Quality Planning and Standards, National Emissions Inventory, Retrieved from http://www.epa.gov/air-emissions-inventories, 2016d.

US Federal Land Manager Environmental Database, Data Wizard, Retrieved from http://views.cira.colostate.edu/fed/DataWizard/, 2016.

van der Werf, G. R., et al., Global fire emissions and the contribution of deforestation, savanna, forest, agricultural, and peat fires (1997-2009), *Atmospheric Chemistry and Physics*, *10*(23), 11,707–11,735, doi:10.5194/acp-10-11707-2010, 2010.

van Donkelaar, A., R. V. Martin, M. Brauer, R. Kahn, R. Levy, C. Verduzco, and P. J. Villeneuve, Global estimates of ambient fine particulate matter concentrations from satellite-based aerosol optical depth: Development and application, *Environmental Health Perspectives*, *118*(6), 847–855, doi:10.1289/ehp.0901623, 2010.

van Donkelaar, A., R. V. Martin, M. Brauer, and B. L. Boys, Use of Satellite Observations for Long-Term Exposure Assessment of Global Concentrations of Fine Particulate Matter, *Environmental Health Perspectives*, *123*(2), 135–143, doi:http://dx.doi.org/10.1289/ehp.1408646, 2015.

van Donkelaar, A., R. V. Martin, M. Brauer, N. C. Hsu, R. A. Kahn, R. C. Levy, A. Lyapustin, A. M. Sayer, and D. M. Winker, Global Estimates of Fine Particulate Matter using a Combined Geophysical-Statistical Method with Information from Satellites, Models, and Monitors, *Environmental Science & Technology*, p. acs.est.5b05833, doi:10.1021/acs.est.5b05833, 2016.

Vinken, G. C. M., K. F. Boersma, D. J. Jacob, and E. W. Meijer, Accounting for non-linear chemistry of ship plumes in the GEOS-Chem global chemistry transport model, *Atmospheric Chemistry and Physics*, *11*(22), 11,707–11,722, doi:10.5194/acp-11-11707-2011, 2011.

Wang, C., J. J. Corbett, and J. Firestone, Improving spatial representation of global ship emissions inventories, *Environmental Science and Technology*, *42*(1), 193–199, doi:10.1021/es0700799, 2008.

World Health Organization, WHO Air quality guidelines for particulate matter, ozone, nitrogen dioxide and sulfur dioxide: Global Update 2005, *Tech. rep.*, World Health Organization, 2006.

Yevich, R., and J. A. Logan, An assessment of biofuel use and burning of agricultural waste in the developing world, *Global Biogeochemical Cycles*, *17*(4), 1095, doi:10.1007/s13398-014-0173-7.2, 2014.

Zender, C. S., Mineral Dust Entrainment and Deposition (DEAD) model: Description and 1990s dust climatology, *Journal of Geophysical Research*, *108*(D14), 82,234, doi:10.1029/2002JD002775, 2003.

Zhang, L., D. J. Jacob, E. M. Knipping, N. Kumar, J. W. Munger, C. C. Carouge, a. Van Donkelaar, Y. X. Wang, and D. Chen, Nitrogen deposition to the United States: Distribution, sources, and processes, *Atmospheric Chemistry and Physics*, *12*(2), 4539–4554, doi:10.5194/acp-12-4539-2012, 2012.

Zhang, R., H. Wang, D. A. Hegg, Y. Qian, S. J. Doherty, C. Dang, P. L. Ma, P. J. Rasch, and Q. Fu, Quantifying sources of black carbon in western North America using observationally based analysis and an emission tagging technique in the Community Atmosphere Model, *Atmospheric Chemistry and Physics*, *15*(22), 12,805–12,822, doi:10.5194/acp-15-12805-2015, 2015.

Appendix A

Supplemental figures

A.1 Regional emission Inventory Spatial Extent

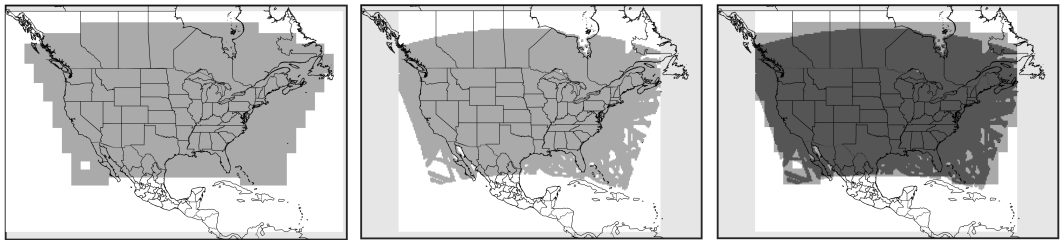

Figure A.1 Geographic extent of the NEI emission inventory at 2° x 2.5°(left), 0.25° x 0.3125°(middle), and overlap (right). White = no emissions, grey = NEI emission, dark grey = overlap

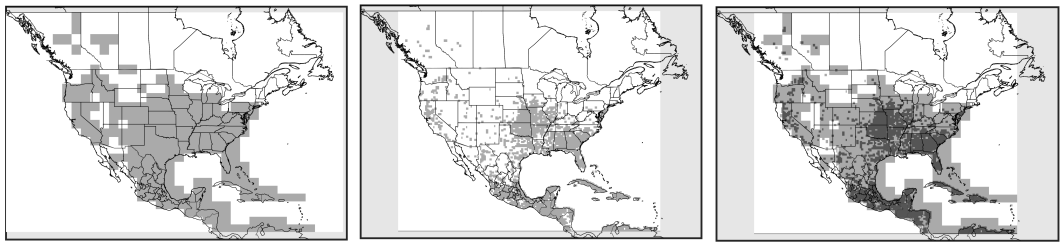

Figure A.2 Geographic extent of the GFED4 emission inventory at 2° x 2.5°(left), 0.25° x 0.3125°(middle), and overlap (right). White = no emissions, grey = GFED emission, dark grey = overlap

A.2 GEOS-Chem Nitric Acid Reduction

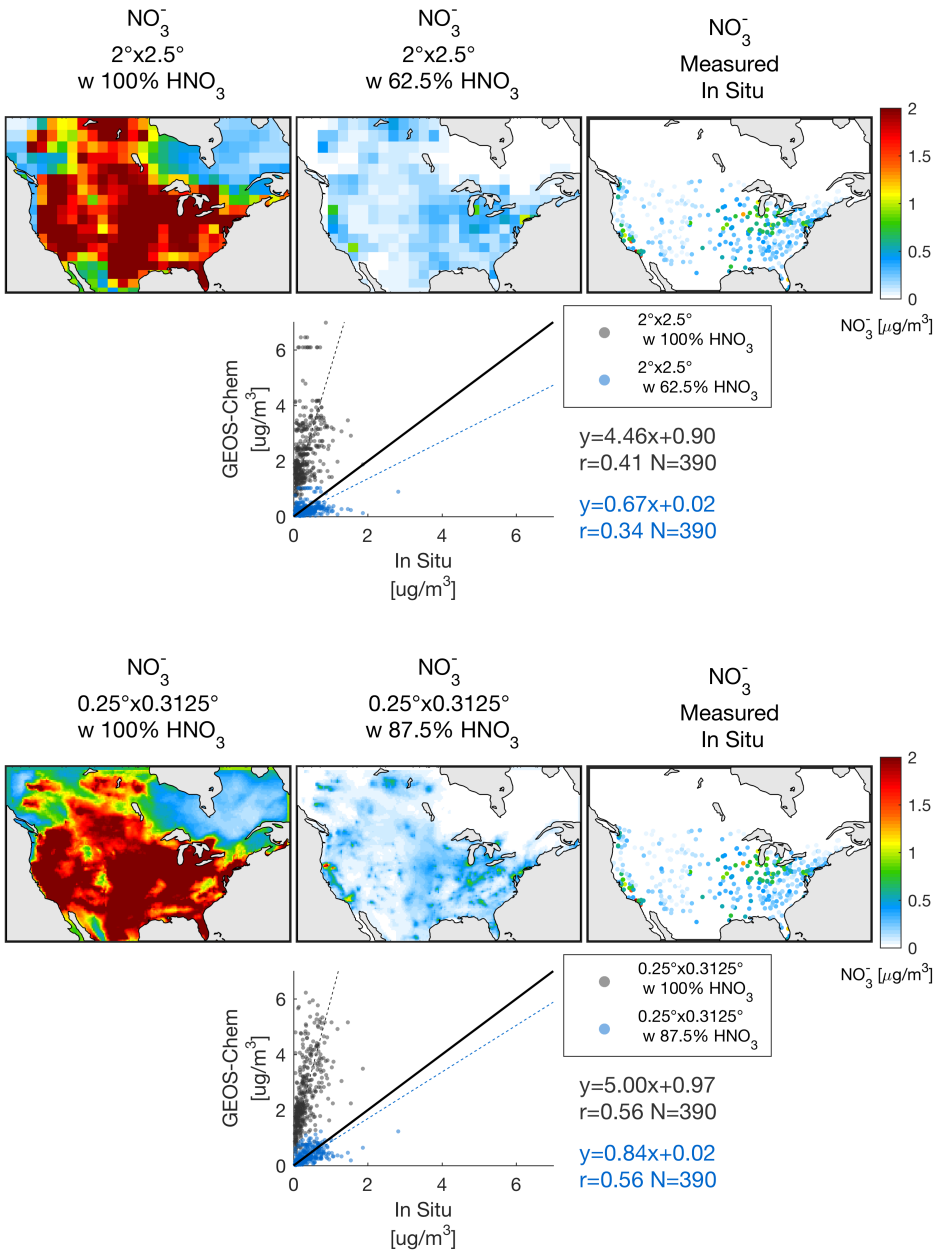

Figure A.3 GEOS-Chem surface NO_3^- concentrations for August 2014 without (far right) and with (middle) artificial reduction in model nitric acid as per *Heald et al.* [2012]. Scatter plot comparison (below) with in situ measured NO_3^- solid black line represents 1:1 relationship, dashed lines represent best fit between simulated and observed values.

Appendix B

Model Run Time

Simulations were performed on the Glooscap cluster of ACENET using 16 CPUs. Values in Table B.1 are for 30-day simulations.

Table B.1 Simulation run time for varying resolution and internal timesteps

Resolution	Simulation	$\Delta T_{transport}$	$\Delta T_{chemistry}$	Run Time
2° x 2.5°	SOA	15 min	30 min	14 hours
0.25°	SOA	10 min	20 min	6 days 17 hours
0.25°	SOA	5 min	10 min	15 days 12 hours
2° x 2.5°	fullchem (no SOA)	15 min	30 min	12 hours
0.25°	fullchem (no SOA)	5 min	10 min	9 days 4 hours

Appendix C

Performance Measures

Correlation coefficient, r:

$$r = \frac{\sum_1^N (C_M - \overline{C_M})(C_O - \overline{C_O})}{\sqrt{\sum_1^N (C_M - \overline{C_M})^2}\sqrt{\sum_1^N (C_O - \overline{C_O})^2}} \tag{C.1}$$

Explained variance:

$$r^2_{0.25} - r^2_{2\text{x}2.5} \tag{C.2}$$